NUMERICAL INVESTIGATION OF BUBBLING FLUIDIZED BED TO BE
USED AS HIGH TEMPERATURE THERMAL ENERGY STORAGE

A THESIS SUBMITTED TO
THE GRADUATE SCHOOL OF NATURAL AND APPLIED SCIENCES
OF
MIDDLE EAST TECHNICAL UNIVERSITY

BY

SERDAR HİÇDURMAZ

IN PARTIAL FULFILLMENT OF THE REQUIREMENTS
FOR
THE DEGREE OF MASTER OF SCIENCE
IN
MECHANICAL ENGINEERING

JULY 2017

Approval of the Thesis:

NUMERICAL INVESTIGATION OF BUBBLING FLUIDIZED BED TO BE USED AS HIGH TEMPERATURE THERMAL ENERGY STORAGE

submitted by **Serdar Hiçdurmaz** in partial fulfillment of the requirements for the degree of **Master of Science in Mechanical Engineering Department, Middle East Technical University** by,

Prof. Dr. M. Gülbin Dural Ünver   _____-_____
Dean, Graduate School of **Natural and Applied Sciences**

Prof. Dr. Raif Tuna Balkan   _____
Head of Department**, Mechanical Engineering**

Prof. Dr. İlker Tarı   _____
Supervisor, **Mechanical Engineering Dept., METU**

Examining Committee Members:

Prof. Dr. Derek K. Baker
Mechanical Engineering Dept., METU   _____

Prof. Dr. İlker Tarı
Mechanical Engineering Dept., METU   _____

Ass't Prof. Dr. Özgür Bayer
Mechanical Engineering Dept., METU   _____

Prof. Dr. Cemal Niyazi Sökmen
Nuclear Engineering Dept., Hacettepe University   _____

Prof. Dr. Cemil Kocar
Nuclear Engineering Dept., Hacettepe University   _____

July 20, 2017

I hereby declare that all information in this document has been obtained and presented in accordance with academic rules and ethical conduct. I also declare that, as required by these rules and conduct, I have fully cited and referenced all material and results that are not original to this work.

Name, Last name : **SERDAR HİÇDURMAZ**

Signature   :

ABSTRACT

NUMERICAL INVESTIGATION OF BUBBLING FLUIDIZED BED TO BE USED AS HIGH TEMPERATURE THERMAL ENERGY STORAGE

Hiçdurmaz, Serdar
MSc., Department of Mechanical Engineering
Supervisor: Prof. Dr. İlker Tarı

July 2017, 92 pages

A thermal energy storage unit designed to be used in a solid particle concentrated solar energy system is analysed with the help of a commercial Computational Fluid Dynamics tool. Hydrodynamics of the bubbling fluidized sand bed of which dimensions are 0.28 m x 1 m x 0.025 m to be used as direct contact heat exchanger are modelled and validated. Geldart B type particles with diameter of 275 micron and density of 2500 kg/m^3 are used in modelling of bubbling fludized sand bed. Syamlal O'Brien drag model with restitution coefficient of 0.99 and specularity coefficient of 0.1 predicts the reported experimental data well in terms of bed expansion ratio, temporal voidage profile and pressure drop across the bed. According to thermal model results, linear relation between interphase heat transfer coefficient and bed temperature is observed. Lifetime of a single bed is found as about 5000 seconds. The obtained thermal results are used to model a particle based storage system for Ivanpah Solar Power Plant. Air Brayton cycle with thermal efficiency of 0.264 can produce 178 MW electricity for 11.22 hours. For Ivanpah, 26304 metric tons silica sand are found to be required for daily storage.

Keywords: Concentrated Solar Power, Thermal Energy Storage, Bubbling Fluidized Bed, Computational Fluid Dynamics, Multiphase Flow

ÖZ

YÜKSEK SICAKLIK ISI ENERJİ DEPOSU OLARAK KULLANILAN KABARCIKLI AKIŞKAN YATAKLARIN SAYISAL İNCELENMESİ

Hiçdurmaz, Serdar
Yüksek Lisans, Makina Mühendisliği Bölümü
Danışman: Prof. Dr. İlker Tarı

Temmuz 2017, 92 sayfa

Katı tanecikli odaklanmış güneş enerjisi sistemlerinde kullanılmak üzere tasarlanan ısı enerjisi depolama ünitesi, hesaplamalı akışkanlar dinamiği yazılımı vasıtasıyla incelenmiştir. Doğrudan temaslı ısı değiştiricisi olarak kulanılan 0.28 m x 1 m x 0.025 m boyutlarındaki kabarcıklı akışkan yatağın hidrodinamiği tasarlanmış ve doğrulanmıştır. 275 mikron çapındaki ve 2500 kg/m^3 yoğunluğundaki Geldart B tipi tanecikler kabarcıklı akışkan yatağın tasarımında kullanılmıştır. Geri sıçrama katsayısının 0.99, yansıtma katsayısının ise 0.1 olarak alındığı Syamlal-O'Brien sürükleme modeli, deneysel olarak elde edilen yatak yükselme oranı, zamana bağlı boşluk kesiti ve yatak boyunca basınç düşümü değerlerini yeterince iyi tahmin edebilmiştir. Isıl tasarım sonuçlarına göre, fazlararası ısı transfer katsayısı ile yatak sıcaklığı arasında doğrusal bir ilişki gözlemlenmiştir. Tek bir yatağın ömrü yaklaşık 5000 saniye olarak bulunmuştur. Elde edilen ısıl sonuçlar, Ivanpah Güneş Güç Santralinde kullanılmak üzere katı parçacık temelli enerji depolama sisteminin tasarımında kullanılmıştır. Verimliliği % 26.4 olan hava Brayton çevrimi 11.22 saat boyunca 178 MW elektrik üretebilir. Ivanpah için, 26304 ton silica kumu günlük enerji depolama için gereklidir.

Anahtar Kelimeler : Odaklanmış Güneş Enerjisi, Isı Enerji Deposu, Kabarcıklı Akışkan Yatak, Hesaplamalı Akışkanlar Dinamiği, Çok Fazlı Akış

ACKNOWLEDGEMENTS

Firstly, I would like to express my gratitude to Prof. Dr. İlker Tarı for his contributions, guidance, and encouragement throughout my graduate studies. It is a privilege to be his student.

Secondly, I am grateful to Prof. Dr. Derek Keith Baker for sharing his vision with me. Being influenced by his engineering perspective is a great chance for early researchers.

I would like also to specially thank Evan Johnson and Serhat Bilyaz for insightful discussions about my thesis.

To a fairer and more livable world,

TABLE OF CONTENTS

LIST OF TABLES

LIST OF FIGURES

FIGURES

CHAPTER 1

INTRODUCTION

1.1. Motivation

In order to meet the increasing energy demand all over the world, efficient, sustainable and environment friendly energy conversion technologies should be engineered. Solar energy is a promising candidate for not only electricity production but also process heat in industrial applications such as calcination as long as it is commercially viable. Available two main options to convert the solar power to useful energy are photovoltaics and solar thermal energy systems (STEs). Photovoltaics, which directly converts sunlight to DC electricity by means of semiconductors, can operate with direct, diffuse and reflected radiation whereas STE is in need of direct radiation. Solar photovoltaics have been commercially available since mid-1900s and module prices have decreased significantly for the last decade, as seen in Figure 1. The major problem with PV technology besides the conversion efficiency is the difficulties in providing uninterrupted energy supply to grid in large scales due to high energy storage costs. Concentrated solar power (CSP) systems, also called solar thermal electricity, have the chance of competing against significant price reductions in photovoltaics thanks to possibility of easy and cheap integration of energy storage options into the system. Main advantage of CSP systems is the ability of storing the heat directly, which enables sensible and latent heat storage, and chemical energy storage. Thereby, electricity is produced continuously depending on the grid demand.
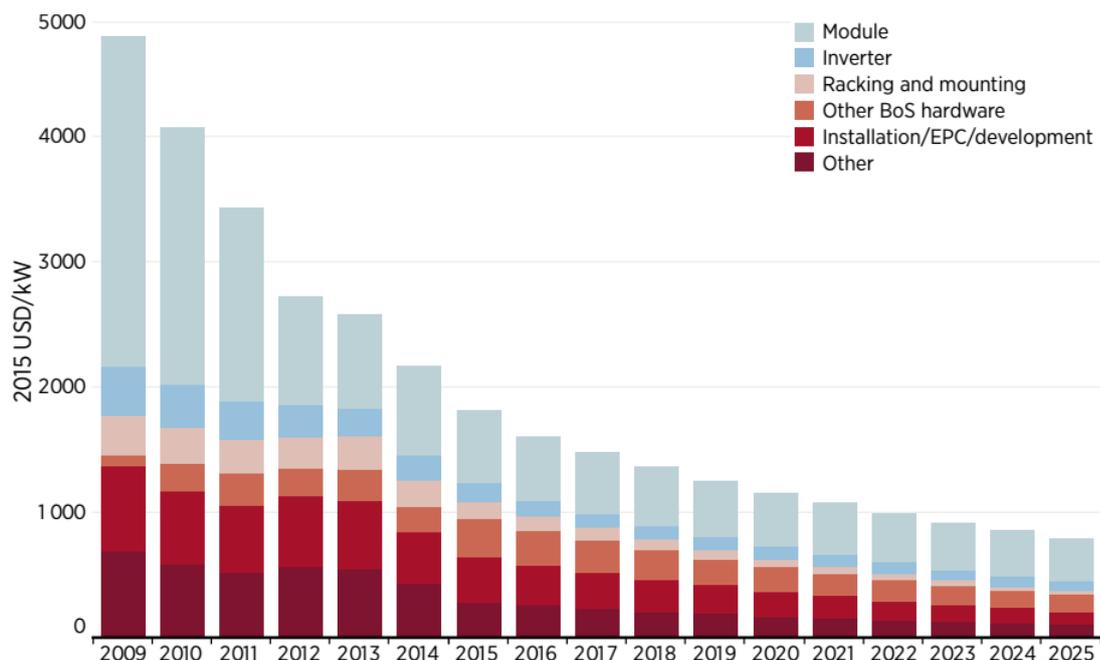
Figure 1. Global weighted average total system costs breakdown of utility-scale solar PV systems, 2009-2025 [1]

Moreover, integration of storage systems into CSP plants increases capacity factor significantly. Considering that imported natural gas, petroleum and coal constitute 31%, 30% and 17% of the Turkey's primary energy supply, respectively, Turkey should exploit renewable energy sources to decrease its energy dependence to foreign countries [2]. As seen in Figure 2, south of Turkey has good DNI resources. In other words, conventional power plants can be replaced by CSP plants in these high DNI regions. In this study, it is primarily aimed to model a thermal energy storage unit which can be integrated into CSP plants to overcome intermittency and buffer fluctuations in energy supply.
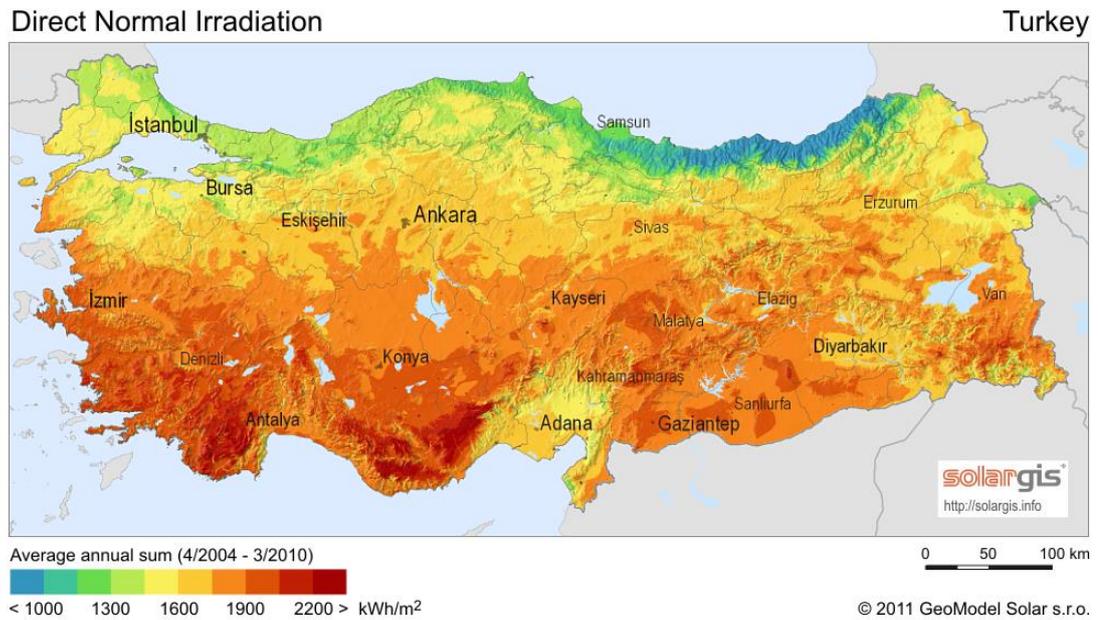
Figure 2. Turkey Direct Normal Irradiation (DNI) resource map [3]

1.2. Concentrated Solar Power Systems

Concentrated solar power applications can be classified according to temperature requirement of the related industry. Low temperature applications generally focus on daily use such as water heating and solar cooling for household applications. Flat plate collectors and evacuated tube collectors, which can generally operate up to 100 $^{\circ}$C, are common examples. Desalination of the saltwater, distillation and solar drying require more heat to evaporate water or to remove the moisture and can be considered as medium temperature applications. To make use of solar heat in industrial process heat applications like direct steam generation (DSG), synthesizing chemicals, pre-heating, tobacco etc., different design approaches are still under development [4]. Solar Heat for Industrial Process (SHIP) can be grouped as low (T <150 $^{\circ}$C), medium (150 $^{\circ}$C < T < 400°C) and high temperature (T > 400 $^{\circ}$C) applications [5]. For utility-scale electricity production, a bunch of mirrors are used to concentrate the sunlight to a focal

point or a focal line. High temperature CSP systems can be divided into two main groups: line focus and point focus systems.

1.2.1. Line Focus Systems

In line focus systems, sunlight is reflected to a pipe through which heat transfer fluid passes and uniform temperature distribution at the outer surface of the pipe is aimed to be achieved. Parabolic Trough Collector (PTC), which is the well-known example of line focus systems, is the most mature technology among concentrated systems as of 2017 in which, parabolic shaped mirror reflectors track the sun's position during the daytime. PTCs are single - axis tracking systems with a concentration ratio of around 80. Geometrically, concentration ratio is the ratio of collector (reflector) aperture area to the receiver (absorber) outer area. The higher the concentration ratio, the higher the temperature in the absorber. PTCs operates at temperatures up to 500 ºC depending on their concentration ratios and the type of heat transfer fluid (HTF). Synthetic oils, molten salts, steam and air are the typical HTFs used in PTCs. As a thermodynamic cycle, Steam-Rankine cycle is suitable for PTC electricity generation applications. Another example of line focus systems is Linear Fresnel Collector (LFC), which is very similar to PTC in terms of operating conditions. Single axis flat mirrors as a reflector track the sun and reflects sunlight to absorber, which is fixed. Investment cost of LFCs is lower compared to that of LFCs but it is less efficient.

1.2.2. Point Focus Systems

In point focus systems, higher concentration ratios than the ones in line focus systems can be achieved, which brings along higher absorber temperatures. As seen in Figure 3, as absorber temperature increases, Carnot efficiency of the power cycle increases; however radiative and convective losses dominate the receiver efficiency at higher

temperatures. Hence, for each absorber temperature, which is a design parameter, and DNI data, there is an optimum concentration ratio. Solar Towers and Dish Collectors are two available options for point focus systems. In Solar Towers, the solar irradiation reflected by two axis tracking heliostats to the point-like hot spot located at the top of the receiver heats the HTF. Depending on physical limitations and characteristics of the HTF, the maximum temperature at the focal area varies between 600°C and 1100°C. Both steam and gas (air, CO_2) cycles can be employed in power generation from tower systems in which the common heat transfer fluids are molten salts, steam and air. In Table 1, some demonstrational, experimental and commercial scale solar towers, which are operational as of 2017, are presented. As observed, thermal energy storage capability of the power plants are limited to daily storage for now.

Other option for point focus systems is Dish Collector, in which the receiver is mounted at the focal point of hemispherical shaped reflector. In dish collectors, concentration ratios of 1000 and above can be reached, along with absorber temperatures of approximately between 700 ^{o}C and 1000°C. Usually, a Stirling engine placed into the focal point of a dish collector is activated by the concentrated sunlight. However, this technology is not mature yet and still under development.

1.3. Energy Storage Techniques for CSP applications

Thermal Energy Storage (TES) systems need to be further developed for successful deployment of CSP systems due to intermittency of the solar resource. CSP systems coupled with TES enable the dispatchability in electricity production. Currently available options can be grouped under three main categories, which are latent, sensible and thermochemical heat storage.
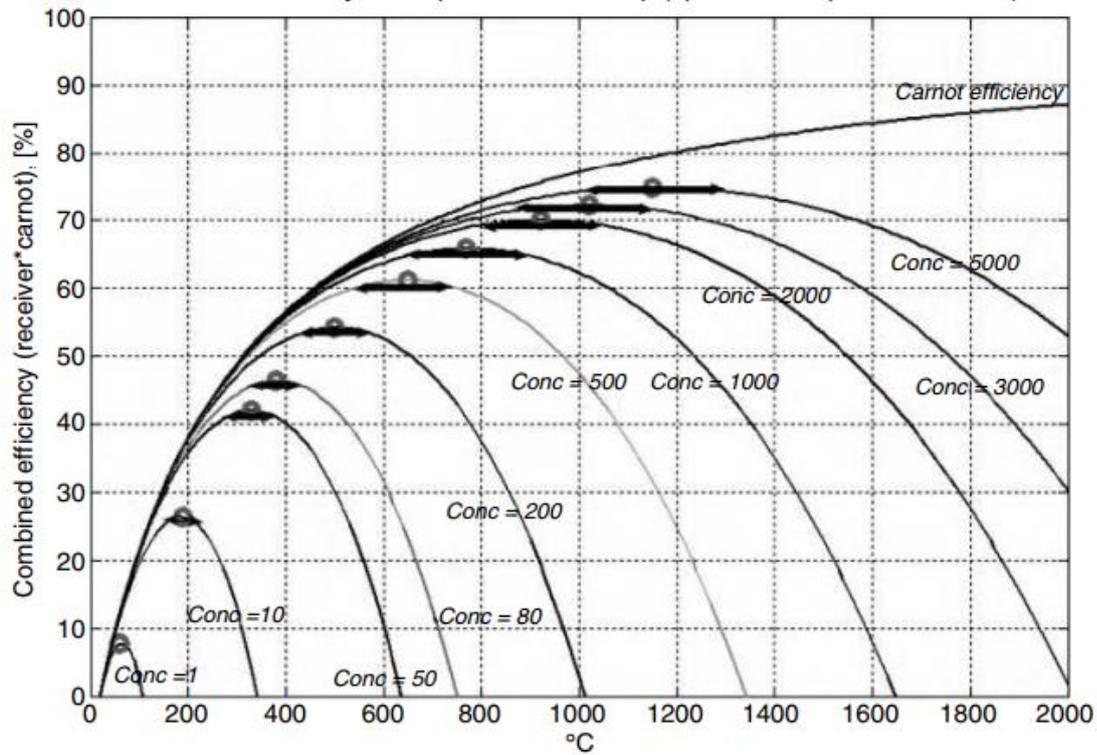
Figure 3. Combined efficiency of the receiver and power cycle. Direct insolation is 770 W/m^2 , ambient temperature of 20 ºC gray and diffuse receiver surface as given in [6]

Direct TES systems, in which the same material is used both as HTF in receiver of the solar tower and as the storage medium, are advantageous compared to indirect TES systems, in which distinct materials are used for HTF and storage requiring additional heat exchangers for TES. Physical limitations like thermal stability at high temperatures or freezing risk of HTF limit the use of direct TES systems in many applications.

As a sensible heat storage, two tank molten salt storage system, of which schematic view is seen in Figure 4, is the state-of-art technology available for CSP thermal energy storage. Molten salt can be used in direct TES systems, as seen in Table 1, in solar towers,

whereas in most PTC systems, indirect TES system is preferred to eliminate freezing risk of molten salt, resulting from relatively low concentration ratios [7].

Table 1. Operational solar towers [8]

Project Name	HTF type	Net Capacity	Storage/Duration
Crescent Dunes Solar /USA	Molten Salt	110 MW	Molten Salt / 10 h
Gemasolar Thermo./Spain	Molten Salt	19.9 MW	Molten Salt / 15 h
IVANPAH Solar/USA	Water	377 MW	-
Khi Solar One/South Africa	Water	50 MW	Saturated Steam / 2 h
Planta Solar 10/Spain	Water	11 MW	Superheated Steam /30 m
Planta Solar 20/Spain	Water	20 MW	Other/1 h
Sierra Sun Tower/USA	Water	5 MW	-
Greenway CSP/Turkey	Water	1 MW	-
Dahan Power Plant/China	Water	1 MW	Saturated Steam/1 h
ACME Solar Tower/India	Water	2.5 MW	-
SunCan Dunhuang/China	Molten Salt	10 MW	Molten Salt / 15 h
Julich Solar Tower/Germany	Air	1.5 MW	Ceramic Heat Sink/1.5 h
Jemalong Solar Ther./Australia	Liq. Sodium	1.1 MW	Liquid Sodium/3 h

In molten salt TES, heated molten salt ($\sim 565\ ^{o}C$) stored in a hot silo is cooled in a heat exchanger to produce steam for power cycle. Cold molten salt ($\sim 290\ ^{o}C$) to be pumped to receiver later is stored in a cold silo. Solar salt comprising of 60 % $NaNO_3$ and 40 % KNO_3, and Hitec^{TM} molten salt comprising of %7 $NaNO_3$, 53% KNO_3 and 40% $NaNO_2$ are examples of commercially used molten salts. Thermal instabilities above 600 ^{o}C, which constraint higher thermal efficiencies, are the limiting factor in use of molten salts in CSP applications. The major advantage of molten salt storage technology is the demonstrated operationality of mechanical components like pumps, valves, piping systems, storage tanks etc.

Thermocline tank, which is another option for sensible thermal energy storage, stores cold and hot material, separated by means of filler material, in the same medium. At

7

charging period, cold fluid located at the bottom of the tank is sent to a heat exchanger to be heated and return to the upper part of the tank. Conversly, hot fluid is cooled in a heat exchanger and pumped to the bottom of the tank at discharging period. The major problem about thermocline is the thermal fatigue resulting from instantaneous temperature change in tank walls.

Phase Change Materials (PCMs) store the thermal energy as latent heat: as heat of fusion, in solid-liquid mixtures or heat of vaporization in liquid-vapor mixtures for further use. The major advantage of the latent heat storage is the isothermal process during charging and discharging. For this reason, PCM is a promising storage technology candidate for dish collectors, which use a Stirling engine for energy conversion.
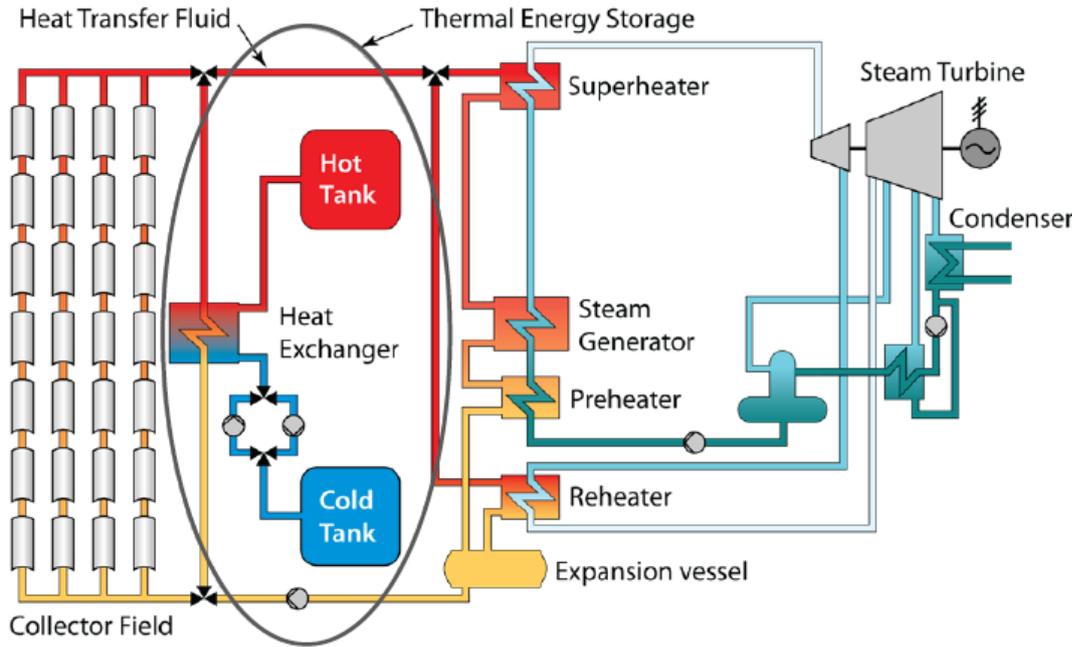
Figure 4. Schematic of PTC power plant, with two tank, molten salt indirect thermal storage [7]

Thermal energy can also be stored as heat of reaction in thermochemical applications. High enthalpy of reaction is required for high energy density. The chemicals should be suitable for long-term cyclic operations. Splitting of $CaCO_3$ into CaO and CO_2, redox reaction of MnO_2 to Mn_2O_3, ammonia decomposition and sulfur (SO_3 and H_2SO_4) cycles are under development for thermochemical storage [9][10].

Although proofs of concept of storage options mentioned above are demonstrated, cost-effective solutions should be developed. For example, molten salt itself constitutes almost half of the installation cost of a two tank molten salt thermal storage unit, as seen in Figure 5. Similarly, for a concrete thermocline storage, the heat exchanger cost is around 57% of the total capital cost [11]. For this reason, affordable storage materials suitable for low-cost heat exchangers is still need to be addressed. Granular materials being available in nature, may be a good solution to this problem since they are thermally stable at elevated temperatures (~ 1000 ºC), non-toxic, very cheap and abundant compared to chemicals and molten salts. They have high energy density (ρC_p), as well.
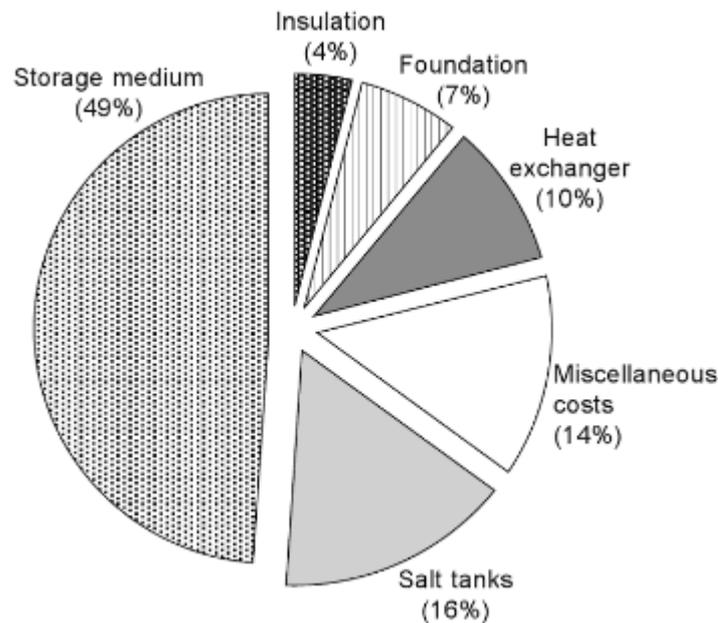
Figure 5. Cost analysis of two tank molten salt indirect storage system for PTC - CSP system [12]

Granular materials can also be used as HTF in a receiver as gas-solid suspensions and as a storage medium even at high temperatures [13].

1.4. Granular Materials as Heat Transfer Fluid and Storage Medium

Granular materials such as sand-like particles are broadly investigated by many researchers to show the feasibility of using these materials as HTF in solar receivers and heat exchangers (HEX). Schematic view of particle based CSP Solar tower is shown in Figure 6. Solid particles in a bulk, firstly, are exposed to sunlight in particle receivers. To elevate their temperatures, various design approaches for particle receivers to maximize the receiver efficiency are available in literature [14]. Heated particles are stored in a hot container for later use. Ma et al. [15] estimated the cost of particle TES system as $<10\$/kWh_{th}$, which is relatively low compared to molten salt TES which costs $30 - 75\$/kWh_{th}$. The material cost is also very low compared to molten salts.

Moreover, most granular particles are thermally stable at elevated temperatures (>1000 °C) whereas molten salts chemically decompose after 600 °C. The main question in particle TES systems is how the heat of particles are recovered efficiently by the working fluid of the power cycle. Warerkar et al. [16] proposed an air to sand HEX for high temperature particle storage, which is seen in Figure 7. The air flows through a porous wall arrangement, across which bulk of particles moves downward and contacts with air. HEX effectiveness of around 0.9 is obtained in experiments. However, cracks at walls are observed after short periods of operation, most probably due to excessive pressure forces.
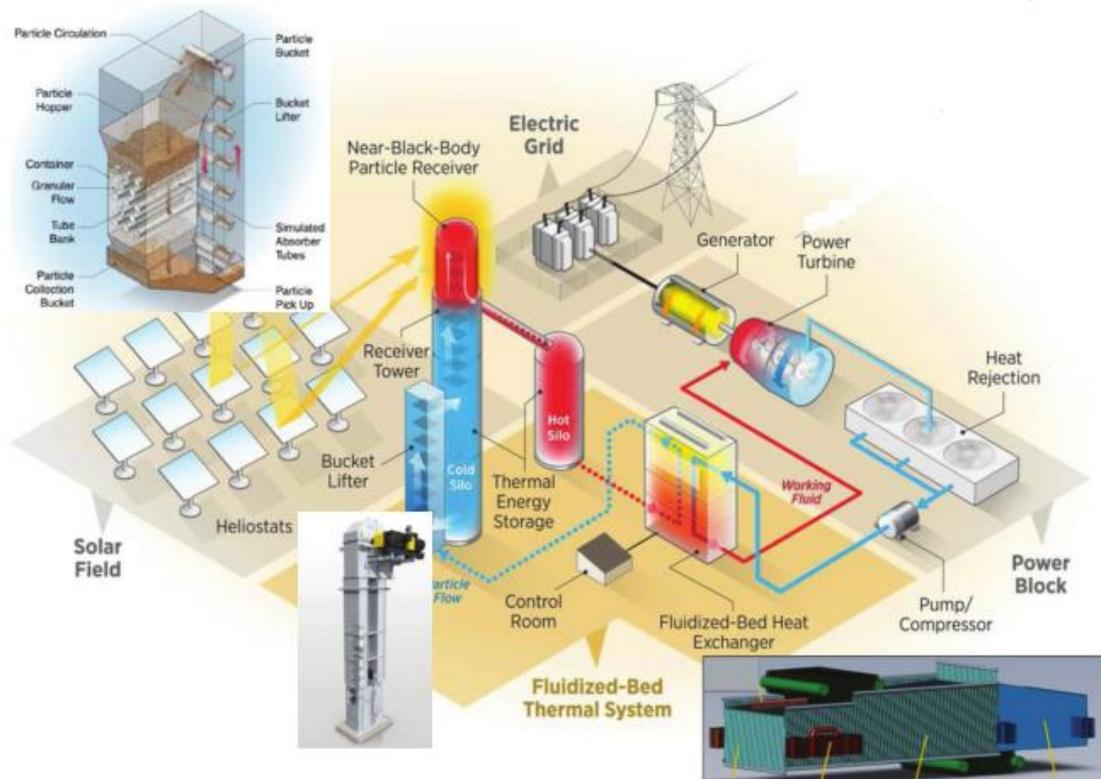
Figure 6. Schematic view of particle CSP power plant [15]

Baumann et al. [17] proposed a moving bed heat exchanger (see Figure 8), which is in a cross flow arrangement. Air flows inside a bundle of tubes, whereas particles in dense regime moves downward. Sintered bauxite particles with a particle density of 3900 kg/m^3 are considered as a granular material in their simulations. Wall to bed heat transfer coefficient for the particle side is found as 400 - 500 W/m^{2}K at the upper side of the tubes. However in this systems, hot particles at high temperatures may corrode the tube surface, which may increase maintenance cost.

In indirect contact heat exchangers, heat transfer is limited due to wall conduction resistance and inadequate heat transfer area. Manufacturing and maintenance cost is too high, which prevents significant reductions in levelized cost of electricity (LCOE) in spite of improved plant capacity factors. To eliminate these drawbacks, a novel

11

direct contact heat exchanger, in which solid and gas phases interact with each other continuously in a bubbling fluidized regime, is proposed in this study.
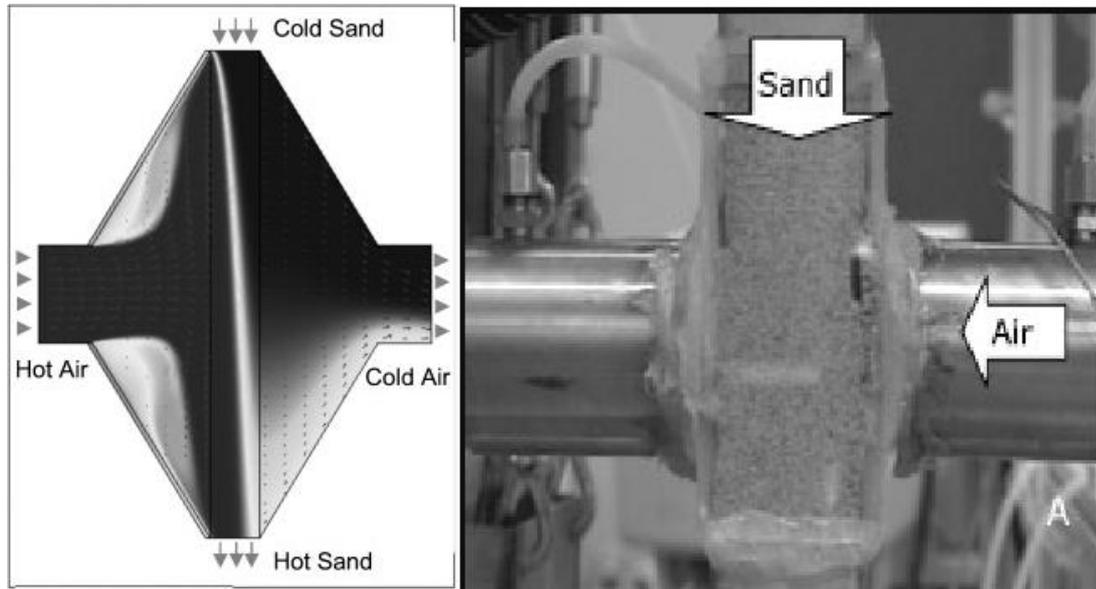
Figure 7. Air to sand heat exchanger [16]

In bubbling regime, mixing of particles is so good that almost a uniform temperature distribution is achieved. Solid particles, used as absorption medium in the particle receiver, are stored in hot containers. By means of distributor plate located at the bottom of the tank, the sand bed is fluidized and stored heat is transferred to the passing air. Thus, sand bed heat exchanger to be used as TES when not fluidized and as heat exchanger when fluidized. The heated air can either be used in an air Brayton cycle or can pass through a steam generator to produce steam for a Rankine cycle. Instead of using mainly 2 tanks as hot and cold, several identical tanks are to be used so that by activating or deactivating the fluidized beds, the turbine inlet temperature can be adjusted.
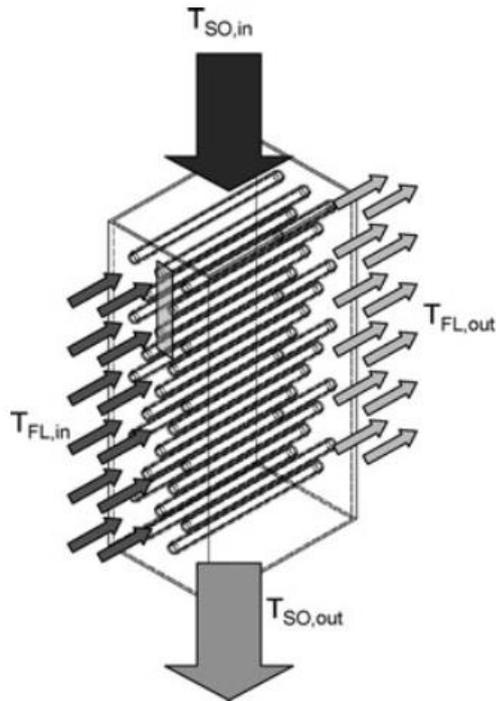
Figure 8. Moving Bed Heat Exchanger model for CSP – TES applications [17]

1.5. Thesis Overview

In this thesis, hydrodynamics and thermal model of a bubbling fluidized bed, which can be regarded as both TES medium and direct contact heat exchanger, is aimed to be modelled numerically with the help of ANSYS Fluent 17.2. Hydrodynamic modelling parameters are investigated in various aspects to better reflect the nature of reality. Taghipour et al. [18] and Vejahati et al. [19] experimental studies are considered for validating the hydrodynamics model of the bed. Heat transfer mechanism between phases are modeled to predict the time variation of air exit temperature to be used in the power block.

In Chapter 1, why CSP systems with thermal energy storage motivate the author is briefly discussed. Distinct CSP technologies are mentioned in terms of their

operationality and intended uses. State-of-art of thermal energy storage systems and proposed particle storage system are introduced.

In Chapter 2, some basics regarding fluidization theory are given to prepare the reader for further chapters.

In Chapter 3, detailed mathematical model including balance equations and closure models are given.

In Chapter 4, computational model and numerical solution approach are discussed in detail. Grid independence study and time step optimization study are carried out to be sure about the accuracy of the results. The accuracy of 2D assumption is investigated

In Chapter 5, hydrodynamics model is validated in terms of pressure drop across the bed, temporal voidage profile inside the bed, and bed height expansion. Distinct model parameters are optimized. Air and sand temperatures varying with time are found. The effect of hydrodynamics on thermal model is investigated. Preliminary system design using obtained thermal results of fluidized sand bed is done, and a what-if study for Ivanpah Solar Power Plant is conducted to show the feasibility the granular material as a storage medium

In Chapter 6, concluding remarks and deductions from study, and the work to be done in the future are mentioned, respectively.

CHAPTER 2

FLUIDIZATION THEORY

Fluidization is the process of transforming granular material into a fluid-like state by the help of a gas or liquid flow fed through a porous medium or a distributor plate. Different flow regimes are observed in fluidized beds in which fluidization occurs depending on the bed geometry, the type of solid particles and the superficial velocity of the fluid. Fluidization regimes are shown in Figure 9, schematically. In absence of a fluid flow, the bed can be considered as a porous medium. At a relatively low flow rate, the fluid percolates through the void between particles that are stationary, known as fixed bed. As superficial velocity increases, the particles start to mobilize vibrationally, which results in a small amount of bed expansion. As one still continues to increase the velocity, a critical point where the drag force exerted by fluid on particle counterbalances the weight of the particles, is observed. This point is named as minimum fluidization condition, and corresponding superficial velocity is called minimum fluidization velocity (U_{mf}). At higher velocities, air bubbles form and coalesce as they rise inside the bed, and solid clusters start to move more vigorously. Such a regime is called as bubbling regime. At still higher velocities, especially in narrow beds, slugging regime is observed, in which air bubbles in big sizes form and particles fall down near the walls of the bed. Chaotic particle motion and bubbles in various shape and sizes are seen in turbulent fluidization regime. The interphase surface between the gas-solid suspension and freeboard disappears. At sufficiently higher velocities where fast fluidization regime and pneumatic conveying are observed, the particles are carried out of the bed. In most fast fluidization operation, a recirculating system is employed. One does not necessarily observe all the regimes

15

discussed above one by one as superficial velocity increases. Depending on particle size, some intermediate regime types may be skipped.

The main intended uses of fluidized beds in industry are coal gasification, gasoline production, metallurgical processes, heat exchangers, coating metal objects, drying of solids, adsorption, synthesis of chemical products, coal combustion, calcination, catalytic cracking and pyrolysis [20]. Fluidization operation provides effective mixing of solid and fluid phases, which results in large contact areas for chemical reactions and enhanced heat and mass transfer. Granular material is easily handled due to its fluid-like behavior. Since fluidized beds can continuously operate, they are suitable for large scale operations.
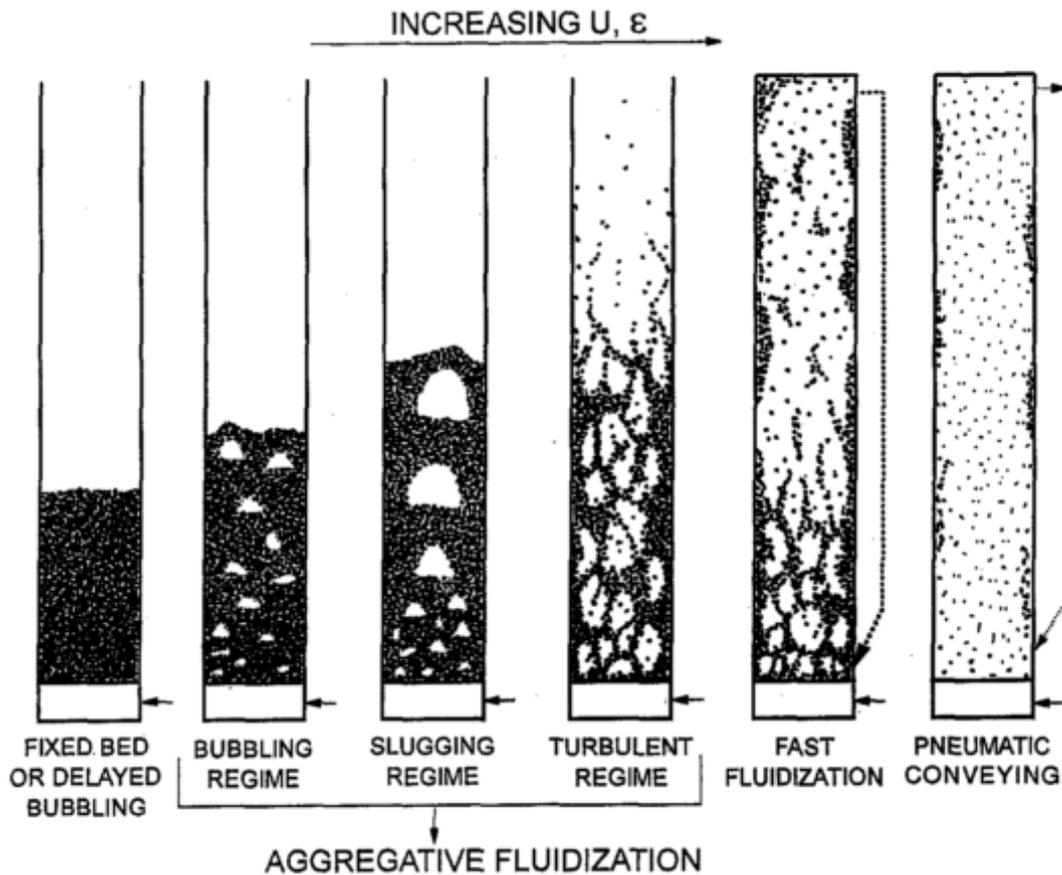
Figure 9. Fluidization regimes [21]

To increase the quality of the fluidization, there are some parameters to be optimized. Firstly, size distribution of particles and particle sphericity should be determined carefully by taking into consideration the intended use. For example, fine particles tend to agglomerate whereas coarse particles are more suitable for spouted bed, which is a tapered vessel with a central core. Fluid-solid density ratio affects the homogeneity of the bed, especially in gas-solid suspensions. The selection of distributor plate, the bed geometry and the type of solid also play a major role in fluidization quality.

2.1. Particle Characterization

Characterization of particles are very important in many aspects like handling, manufacturing and processing. First, a single particle should be characterized in terms of its intrinsic static properties like size, density, sphericity and morphology [22]. An ideal particle is assumed to be perfect sphere. However, in real life, particles are in irregular shapes such as flakes. To define how close the particle is to a perfect sphere, sphericity is used as a metric. It is defined as [22]

$$\phi = \frac{A_{eq}}{A_p} \tag{1}$$

A_{eq} refers to surface area of a perfect sphere of which the volume is equal to particle's one whereas A_p is the particle surface area. For a perfect sphere, ϕ equals to 1 whereas for irregular particles it is always less than 1. Recommended sphericity values for nonspherical particles are present in the literature [20][22]. The equivalent diameter of nonspherical particle is defined as

$$d_s = \left(\frac{6V_p}{\pi}\right)^{1/3} \tag{2}$$

where V_p is the volume of the particle. Having known the particle diameter and density, Geldart [23] classified the particles according to their fluidization ability. In Figure 10, It is seen that particles are classified in terms of mean diameter $(\overline{d_p})$ and

density difference between the phases. Geldart [23] categorized the particles into four main groups.

Geldart C type particles, also known as cohesive particles, have poor fluidization ability because interparticle forces among particles are dominant compared to drag force resulting from gas flow. Particle mixing is so poor that heat and mass transfer is limited. Face powder and flour are typical Geldart C type particles.

Geldart A type particles, which are easily aerated, fluidize smoothly at low velocities. Fluidized beds containing these type of particles undergo relatively high bed expansion before bubble formation. Agglomeration may be observed. Cracking catalysts are typical examples.
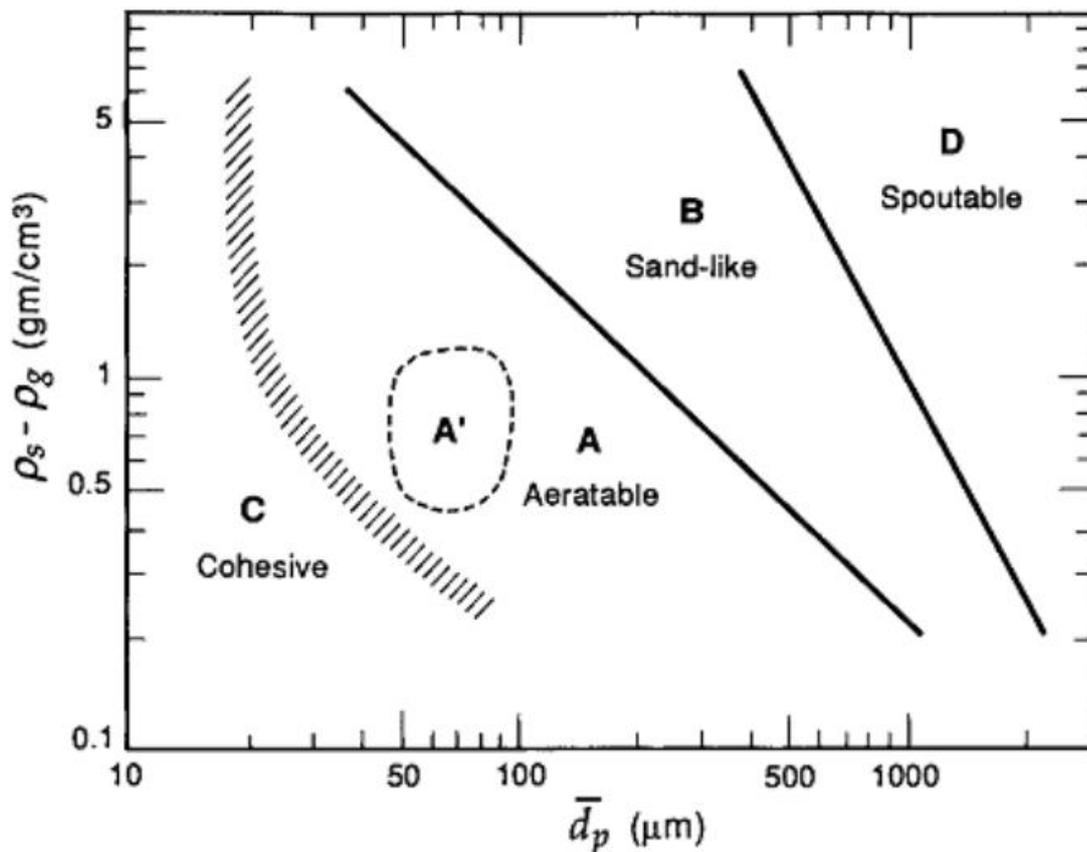
Figure 10. Geldart's [23] particle classification

18

Geldart B type particles, generally named as sand-like particles, fluidize well and bubbles form immediately after the minimum fluidization velocity is reached. Small bubbles located above the distributor plate coalesce and grow as bubbles rise. There is almost linear relation between the bubble size and the distance from distributor. Glass bead and desert sand are representatives of this group.

Geldart D type particles are relatively large and dense ones. A large rate of gas flow is required to fluidize Geldart D particles compared to the other three types. Shallow beds are more suitable to observe bubbles by comparison with deep beds. Roasting coffee beans and gasifying coals are included in this group.

2.2. Fluidization Regime Mapping

In practical applications, the fluidization behavior of gas-solid systems highly depends on the hydrodynamic properties of solid and gas. μ_g, ρ_g, ρ_s which stand for dynamic viscosity of gas, density of gas and density of solid, respectively, are the most prominent properties in mapping the fluidization regimes and used to nondimensionalize the physical quantities like particle diameter and superficial gas velocity as follows :

$$d_s^* = d_s \left(\frac{\rho_g (\rho_s - \rho_g) g}{\mu_g^2} \right)^{1/3} \tag{3}$$

$$u^* = u \left(\frac{\rho_g^2}{\mu_g (\rho_s - \rho_g) g} \right)^{1/3} \tag{4}$$

d_s^* and u^* are non-dimensional particle diameter and non-dimensional superficial gas velocity, respectively. In Figure 11, dependency of fluidization regimes to dimensionless parameters is shown. For gases different from air, d_p^* is recalculated by

19

taking account of gas density to better predict the boundary between Geldart A to B. Bubbling fluidization regime is mostly observed in beds containing in Geldart A and B particles. For operations in which carryover of particles is aimed to be minimized, terminal velocity (U_T) should not be exceeded. Terminal velocity of a particle is the velocity at which all forces acting on a particle like buoyancy and drag are in equilibrium when wall effects are negligible. From fluid dynamics, it is defined as

$$U_T = \left(\frac{4d_s(\rho_s - \rho_g)g}{3\rho_g C_D}\right)^{1/2} \tag{5}$$

where C_D is drag coefficient derived for a single particle floating in a fluid. Many correlations of drag coefficient can be found in literature [24].
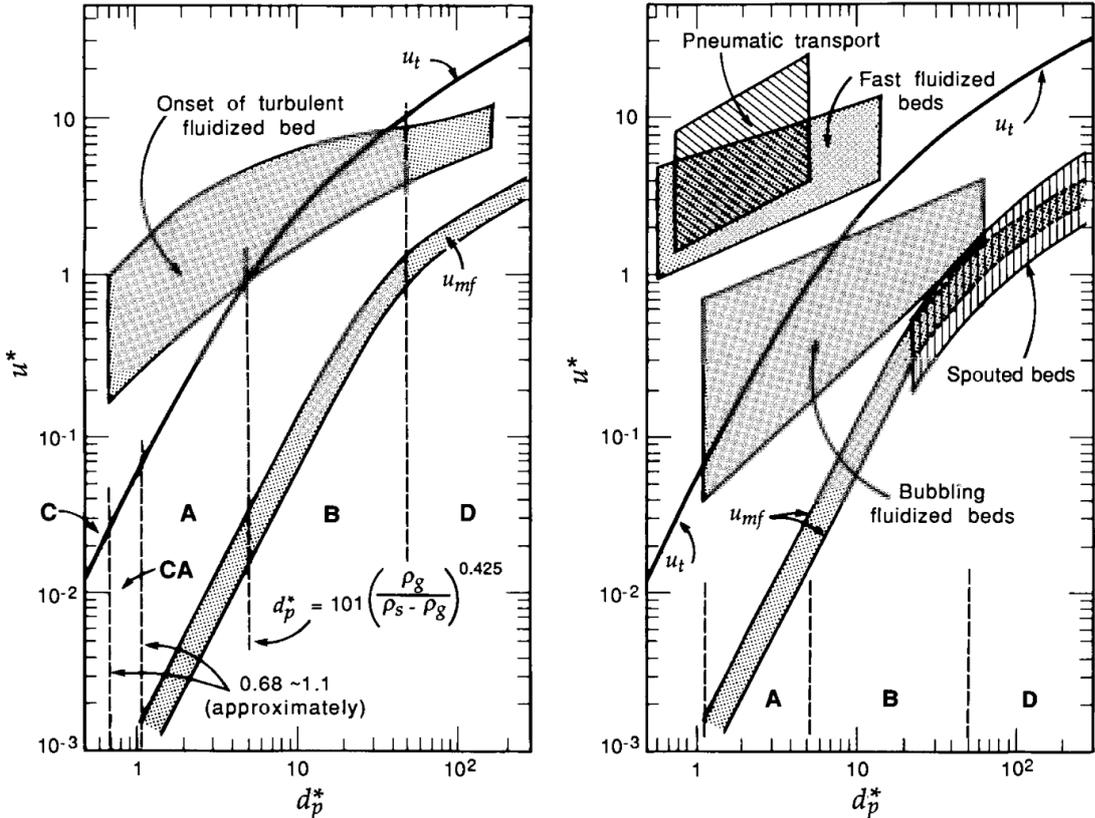
Figure 11. Mapping of Fluidization Regimes [20] according to Geldart classification (A, B, C, CA, D)

20

In designing of bubbling fluidized bed, the superficial gas velocity should be set in such a way that it is not only higher than U_{mf} but also lower than U_T.

CHAPTER 3

CFD MODELLING OF BUBBLING FLUIDIZED BED

Since computational techniques become viable with the advances in computer technology, numerical modelling of multiphase flows has been preferred by many researchers for solving engineering problems. To model gas - solid suspension numerically, two main approaches are proposed in the literature. The first one is the Lagrangian-Eulerian (LE) approach, which considers solid particles moving in a fluid medium as a discrete phase, in which equations of motion are solved individually for each solid particle to predict its trajectory. Various techniques like Direct Numerical Solution (DNS) Method, Lattice-Boltzman Method (LBM), Discrete Element Method (DEM), Direct Simulation Monte Carlo Method (DSMC) and Multiphase Particle in Cell Method (MPPIC) are developed by employing LE approach [25]. The details of these methods are not mentioned here for brevity.

The second and commonly preferred approach is Eulerian-Eulerian (EE). EE approach accepts that both solid and fluid phases are continuous and interpenetrating continuously. Navier-Stokes equations are solved for each phase separately and coupled to each other by employing a volume fraction approach. Here, sufficiently large number of particles are needed to prevent discontinuities in the flow field. Chiesa et al. [26] compared LE and EE approaches and concluded that LE results in less numerical diffusion errors, have higher stability for flows with large particle velocity gradients and are more suitable for poly-dispersed particle systems. Although LE gives very accurate results, computational cost and required storage area are so high that LE is only appropriate for dilute regimes for now, while the fact that there are on the order

of million particles inside the bed must be taken into consideration in fluidized bed simulations.

3.1. Governing Equations

In EE formulation, mass balance, momentum balance and energy balance equations are derived for each phase. A single fluid pressure is shared by all phases. All derivations are done for a system consisting of single gas phase and single mono-dispersed solid phase. The sum of the volume fractions of fluid phase and solid phase is always one.

$$\sum_{m=0}^{M} \varepsilon_m = 1 \qquad (6)$$

The conservation of mass is derived in differential form as [25]

$$\frac{\partial}{\partial t}(\varepsilon_m \rho_m) + \nabla \cdot (\varepsilon_m \rho_m \vec{v}_m) = 0 \qquad (7)$$

The first term on left hand side in Equation (7) represents the rate of mass accumulation in the control volume whereas the second term is the net rate of mass flux crossing the control volume boundaries. Since there is no mass generation, mass sink or mass transfer between phases in this study, the right hand side reduces to 0. "m" stands for both gas and solid phases. For gas and solid phases, momentum equations are as follows [25]

$$\frac{\partial}{\partial t}\left(\varepsilon_g \rho_g \vec{v}_g\right) + \nabla \cdot \left(\varepsilon_g \rho_g \vec{v}_g \vec{v}_g\right)$$
$$= -\varepsilon_g \nabla P_g + \nabla \cdot \overline{\overline{\tau}}_g - \vec{I}_{gs} + \varepsilon_g \rho_g \vec{g} \qquad (8)$$

$$\frac{\partial}{\partial t}(\varepsilon_s \rho_s \vec{v}_s) + \nabla \cdot (\varepsilon_s \rho_s \vec{v}_s \vec{v}_s)$$
$$= -\varepsilon_s \nabla P_g - \nabla P_s + \nabla \cdot \overline{\overline{\tau}}_s - \vec{I}_{sg} + \varepsilon_s \rho_s \vec{g} \qquad (9)$$

24

where $\vec{\tau}$ is the phase viscous stress tensor. $\vec{I}_{gs}$ and $\vec{I}_{sg}$ are the momentum transfer between phases and sum of these quantities are always zero. $\varepsilon\rho\vec{g}$ is the gravitational body force. P_s is solid pressure derived from kinetic theory of granular flow. The first term on left hand sides of both Equations (8) and (9) is the net rate of momentum change in the control volume whereas the second term is the net rate of convectional momentum transfer. The subscripts "g" and "s" stand for gas and solid, respectively. Johnson et al. [27] investigated the interaction forces between solid and gas phases in detail. Drag force, resulting from velocity differences between phases; Basset force and virtual (added) mass force, due to acceleration or deceleration of phases; lift force, caused by fluid- velocity gradient; Magnus effect, stemming from a spinning body in a fluid and the forces resulting from temperature and pressure gradients are the prominent interaction forces. For dense fluidized beds with gas solid suspensions, drag force is dominant over the others, so only drag force is modeled as an interaction force in this study. Energy balance equation for both phases is shown in Equation (10).

$$
\begin{aligned}
\frac{\partial}{\partial t}(\varepsilon_m \rho_m h_m) &+ \nabla.(\varepsilon_m \rho_m \vec{u}_m h_m) \\
&= \varepsilon_m \frac{\partial P_q}{\partial t} + \overline{\overline{\tau_m}}:\nabla \vec{u}_m - \nabla.\vec{q}_m + Q_{int}
\end{aligned}
\tag{10}
$$

The first term on right hand side is interfacial flow work term at constant volume. The second term is the heat production due to viscous dissipation. The third term is the conductive heat flux whereas the last term is interphase heat exchange between phases. The radiative heat transfer between solid particles is not considered. Enthalpy is calculated by using variable specific heat capacity approach. All thermal properties of the phases are modeled as temperature dependent.

3.2. Interphase Momentum Transfer

In bubbling fluidized beds, the most important momentum transfer mechanism between phases is the drag force. Drag is the mechanical force, which is exerted by fluid to solid body in the same direction with the fluid motion.

25

$$\vec{I}_{gs} = F_{gs}(\vec{v}_g - \vec{v}_s) \tag{11}$$

Various drag models to predict the flow behavior are present in literature. Syamlal and O'Brien [28][29] proposed a drag correlation formula by taking the terminal velocity of the solid particle into account. The details of Syamlal – O'Brien drag formula is presented in Equations (12)-(17) below.

$$F_{gs} = \frac{3\varepsilon_s\varepsilon_g\rho_g}{4d_s v_{r,s}^2} C_D |\vec{v}_s - \vec{v}_g| \tag{12}$$

In Equation (12), C_D represents multiparticle drag coefficient.

$$C_D = \left(0.63 + 4.8\sqrt{\frac{v_{r,s}}{Re_s}}\right)^2 \tag{13}$$

in which Reynolds number for the particles is defined as

$$Re_s = \frac{\rho_g d_s |\vec{v}_s - \vec{v}_g|}{\mu_g} \tag{14}$$

In Equation (13), $v_{r,s}$ is the terminal velocity correlation, and defined as

$$v_{r,s} = 0.5 \left(A - 0.06Re_s + \sqrt{(0.06Re_s)^2 + 0.12Re_s(2B - A) + A^2}\right) \tag{15}$$

where,

$$A = \varepsilon_g^{4.14} \tag{16}$$

$$B = c\varepsilon_g^{1.28} \quad \text{for } \varepsilon_g \leq 0.85$$

$$B = \varepsilon_g^d \quad \text{for } \varepsilon_g > 0.85 \tag{17}$$

The constants c and d are 0.8 and 2.65, by default. Syamlal and O'Brien [28][30] enhanced the drag correlation mentioned above by replacing default c and d values by the modified experimental values. The resulting new semi-emprical correlation is named as parameterized Syamlal-O'Brien drag formula. This enhancement assures that the drag force determined analytically and experimentally gives the same result at

minimum fluidization. By doing so, it is aimed to better predict the instantaneous bed height of the bed at minimum fluidization condition.

Archimedes Number (Ar) which is the ratio of forces resulting from density differences to viscous forces is defined as [28]

$$Ar = \frac{3}{4} C_D \left(\frac{Re_s}{v_{r,s}}\right)^2 \tag{18}$$

Note that C_D is a function of A and B which are defined in Equations (16) and (17). At terminal settling velocity, the drag force counterbalances the buoyancy force. Inserting Equation (13) into Equation (18) and solving for Re_s yields

$$\frac{Re_s}{v_{r,s}} = \left[\frac{\left(4.8^2 + 2.52\sqrt{4Ar/3}\right)^{0.5} - 4.8}{1.26}\right]^2 \tag{19}$$

The right hand side of Equation (19) is only the function of Ar, so it is called as Ar^*. Garside and Al-Dibouni [31] proposed velocity-voidage correlation.

$$\frac{v_{r,s} - A}{B - v_{r,s}} = 0.06 Re_s \tag{20}$$

Inserting Equation (19) into Equation (20) and solving for $v_{r,s}$ yields

$$v_{r,s} = \frac{A + 0.06 B Ar^*}{1 + 0.06 Ar^*} \tag{21}$$

After assuming c and finding d that depends on c by Equation (22), Equations (15)-(22) are solved iteratively to find the modified c and d values. Void fraction and Re_s at minimum fluidization are considered in iterative process.

$$d = 1.28 + log_{0.85} c \tag{22}$$

Gidaspow et al. [32] investigated the kinetic theory applied to hydrodynamics of circulating fluidized beds and proposed a drag formula for gas-solid suspensions. It is combination of Wen and Yu [33] drag formula, based on empirical correlation, and Ergun [34] equation, derived for packed bed.

$$\varepsilon_g \geq 0.8 \qquad\qquad F_{gs} = \frac{3}{4} C_D \frac{\varepsilon_s \varepsilon_g^{-1.65} \rho_g}{d_s} |\vec{v}_s - \vec{v}_g|$$

(23)

$$\varepsilon_g < 0.8 \qquad\qquad F_{gs} = 150 \frac{\varepsilon_s^2 \mu_g}{\varepsilon_g d_s^2} + 1.75 \frac{\varepsilon_s \rho_g}{d_s} |\vec{v}_s - \vec{v}_g|$$

where

$$C_D = \frac{24}{\varepsilon_g Re_s} \left(1 + 0.15 \left(\varepsilon_g Re_s \right)^{0.687} \right)$$

(24)

Di Felice [35], Arastoopour et al. [36], Zhang et Reese [37], Gibilaro et al.[38], Hill et al. [39] also provided drag correlations to model the gas-solid suspensions numerically.

3.3. Phase Viscous Stress Tensor

Viscous stress tensor for gas phase ($\bar{\bar{\tau}}_g$) appearing in momentum balance equation, Equation (8), is defined in Newtonian form as [40]

$$\bar{\bar{\tau}}_g = \varepsilon_g \mu_g \left(\nabla \vec{v}_g + \nabla \vec{v}_g^T \right) + \varepsilon_g \left(\lambda_g - \frac{2}{3} \mu_g \right) \nabla . \vec{v}_g \bar{\bar{I}}$$

(25)

where λ_g is the bulk viscosity of gas, and $\bar{\bar{I}}$ is the identity matrix. For the solid phase, rheology is more complicated because particles themselves are not viscous but the bulk of them can be accepted as viscous. Depending on the granular activity, closure models to describe the nature of the viscous stress are developed for both dilute and dense regions of the gas - solid flow. In Figure 12, schematic representation of granular viscous behavior is presented. In dilute regions, particles freely move and fluctuate, and do not interact with each other. Stresses resulting from this type of viscous dissipation is named as kinetic. As volume fraction of particles increases, they may collide with each other randomly; and particle-particle collisions become the prominent momentum transfer mechanism among particles. This is called as collisional part of the stress. Lun et al. [41] proposed a comprehensive formulation to

28

model the kinetic and collisional stress by considering the kinetic theory of granular flows, which is analogous to Boltzmann's kinetic theory of gas. At very high solid volume fractions near to maximum packing limit, the friction among sliding particles come to the forefront. It results in frictional contribution to solid stress.

Viscous stress tensor for the solid phase is defined as

$$\bar{\bar{\tau}}_s = \varepsilon_s \mu_s (\nabla \vec{v_s} + \nabla \vec{v}_s^T) + \varepsilon_s \left(\lambda_s - \frac{2}{3} \mu_s \right) \nabla . \vec{v_s} \bar{\bar{I}} \tag{26}$$

Before deriving the solid shear viscosity, granular temperature concept should be discussed, first. Granular Temperature like the gas temperature represents the average kinetic energy resulting from vibrating nature of the grains but the mass of the particle is not included in the formulation. It is defined as

$$\Theta_s = \frac{1}{3} \langle C^2 \rangle \tag{27}$$

C is the fluctuating velocity, which is the difference between the instantaneous and hydrodynamic velocity, and triangular parenthesis refer to spatial averaging over the velocity space [42]. The fluctuating velocity is due to random grain motion. The granular energy is produced through viscous dissipation and dissipated as heat due to inelastic particle collisions. Ding et Gidaspow [43] derived general transport equation for granular energy from granular kinetic theory.

$$\frac{3}{2} \left[\frac{\partial}{\partial t} (\rho_s \varepsilon_s \Theta_s) + \nabla . (\rho_s \varepsilon_s \vec{v_s} \Theta_s) \right]$$
$$= (P_s \bar{\bar{I}} + \bar{\bar{\tau}}_s) : \nabla \vec{v_s} + \nabla . (k_{\Theta_s} \nabla \Theta_s) - \gamma_{\Theta_s} + \phi_{gs} \tag{28}$$

The first and second terms of the left hand side of Equation (28) represent the net accumulation and net flux of the granular energy to the boundaries, respectively. The first term on the right hand side is the granular energy produced through viscous dissipation; the second one is the diffusion of the granular energy, where k_{Θ_s} is granular diffusivity; γ_{Θ_s} is the dissipation of granular energy due to inelastic particle collisions and ϕ_{gs} is the granular energy exchange between phases.
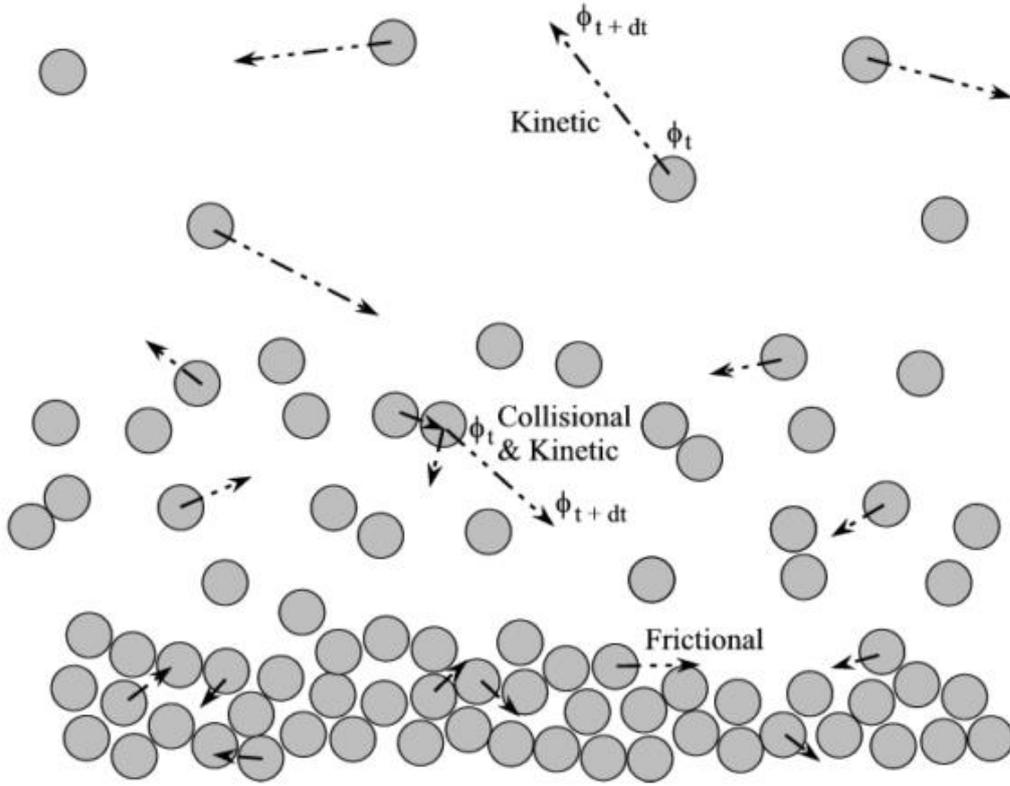
Figure 12. Kinetic, collisional and frictional contribution to the viscous dissipation [44]

van Wachem et al. [45] states that granular energy is produced and dissipated locally for dense flows so that convective and diffusive terms can be neglected. This simplification reduces the computational cost around 20%. In this study, algebraic granular temperature model is preferred, accordingly. Hence, the granular temperature equation reduces to

$$0 = \left(P_s \bar{\bar{I}} + \bar{\bar{\tau}}_s\right) : \nabla \vec{v_s} - \gamma_{\Theta_s} \qquad (29)$$

Lun et al. [41] proposed granular energy dissipation formulation by considering uniform, smooth, spherical and inelastic particles.

$$\gamma_{\Theta_s} = \frac{12(1 - e_{ss}^2)g_{0,ss}}{d_s\sqrt{\pi}}\rho_s\varepsilon_s^2\Theta_s^{3/2} \tag{30}$$

The particle-particle restitution coefficient (e_{ss}) describes the elasticity of the particle collisions. e_{ss}=1 corresponds fully elastic collision and e_{ss}=0 is for fully inelastic collision. $g_{0,ss}$ is the radial distribution function, which is a correction factor modifying the probability of the collisions between particles in dense regime. For monodispersed granular phase, it is defined as [40]

$$g_{0,ss} = \left[1 - \left[\frac{\varepsilon_s}{\varepsilon_{s,max}}\right]^{1/3}\right]^{-1} \tag{31}$$

Solids pressure or granular pressure (P_s) in Equations (28) and (29) is derived from kinetic theory. It is defined as [46]

$$P_s = 2\rho_s(1 + e_{ss})\varepsilon_s^2 g_{0,ss}\Theta_s \tag{32}$$

Within solids pressure formulation, only kinetic and collisional contribution are included. The frictional contribution is taken into consideration when the solid volume fraction exceeds a critical value ($\varepsilon_{s,min}$),which is set to 0.5, by default. Physically, there is an upper limit of solid volume fraction due to irregular shape of granular materials. This limit is called as maximum packing limit ($\varepsilon_{s,max}$) and determined experimentally. Solid shear viscosity and solids pressure are recalculated, accordingly [40].

$$P_s = P_{kin+col} + P_{friction} \tag{33}$$

$$\mu_s = \mu_{kin+col} + \mu_{friction} \tag{34}$$

Johnson and Jackson [40][47] proposed a frictional pressure formula defined as

$$P_{friction} = 0.1\varepsilon_s\frac{(\varepsilon_s - \varepsilon_{s,min})^2}{(\varepsilon_{s,max} - \varepsilon_s)^5} \tag{35}$$

$$\mu_{friction} = P_{friction}\sin\varphi \tag{36}$$

$\mu_{friction}$ is the frictional viscosity derived to account for the frictional stress caused by the contacting particles in dense regimes. φ is the angle of friction between sliding particles. It is low for spherical, smooth and coarse particles and high for sticky, sharp

and fine particles. Typically, it is between 15° and 50° [44]. $\mu_{kin+col}$ is derived from kinetic theory and defined as [40]

$$\mu_{kin+col} = \varepsilon_s \rho_s d_s \sqrt{\Theta}[X + Y]$$

$$X = \frac{4}{5} g_{0,ss}(1 + e_{ss})\varepsilon_s \tag{37}$$

$$Y = \frac{\pi}{6(3 - e_{ss})}\left[1 + \frac{2}{5}(1 + e_{ss})(3e_{ss} - 1)\varepsilon_s g_{0,ss}\right]$$

Granular material has ability to resist to contraction and expansion thanks to bulk viscosity of solid phase which is defined by Lun et al. [41].

$$\lambda_s = \frac{4}{3}\varepsilon_s^2 g_{0,ss}\rho_s d_s(1 + e_{ss})\sqrt{\frac{\Theta_s}{\pi}} \tag{38}$$

Finally, solid shear stress at walls is redefined as a boundary condition.

$$\bar{\bar{\tau}}_s = \frac{\pi\sqrt{3\Theta}\,\phi\rho_s g_{0,ss}U_{slip}}{6} \tag{39}$$

where U_{slip} is the particle slip velocity parallel to the wall and ϕ is the specularity coefficient. The specularity coefficient ranges from 0 to 1, with a zero value for perfectly specular collisions (particles slipping freely at walls) and a value of unity for perfectly diffuse collisions (particles sticking or not slipping at walls) [48].

3.4. Interphase Heat Transfer

The heat exchange between phases has a crucial role in thermal modelling of fluidized beds, and it can be written as

$$Q_{int} = hA_i(T_s - T_g) \tag{40}$$

because the driving force of the heat transfer between phases is convection whereas conduction is dominant for particle to particle heat transfer. Radiation among particles are neglected since no large temperature gradients inside the bed are expected due to good particle mixing characteristics of the bubbling beds. In Equation (40), Q_{int} is

volumetric rate of heat transfer, h is the convective heat transfer coefficient, and A_i is interfacial area concentration, which is defined as [40]

$$A_i = \frac{6\varepsilon_s \varepsilon_g}{d_s} \tag{41}$$

Gunn [49] proposed a Nusselt correlation for granular flows, which is applicable to a void fraction range of 0.35 - 1 and a Reynolds Number of up to 10^5.

$$Nu_s = (7 - 10\varepsilon_s + 5\varepsilon_s^2)\left(1 + 0.7Re_s^{0.2}Pr^{1/3}\right) + (1.33 - 2.4\varepsilon_s + 1.2\varepsilon_s^2)Re_s^{0.7}Pr^{1/3} \tag{42}$$

The relation between Nu and h is defined as

$$Nu_s = \frac{hd_s}{k_g} \tag{43}$$

where k_g is gas conductivity.

Balance and closure equations discussed above in detail are to be used to simulate the gas – solid multiphase flow in the computational domain via numerical algorithm built in ANSYS Fluent 17.2. Eulerian- Eulerian formulation includes most semi-empirical correlations and assumptions to simplify the complex nature of granular flow. Hydrodynamic and thermal model validation is a must for further modelling. In the next chapter, numerical model and solution approach are discussed in detail.

CHAPTER 4

MODEL DEVELOPMENT

In order to achieve heat recovery from hot solid particles that are heated up during daytime, a bubbling fluidized sand bed is modeled. This heat recovery system can also be regarded as a direct contact heat exchanger, which both cold and hot fluid mediums are interpenetrating continuously. In this chapter, numerical model of the bubbling fluidized sand bed is discussed in detail.

4.1. Numerical Model

The physical components of the system are mainly, the bed geometry, solid particles and fluidizing gas.

4.1.1. Bed Geometry

The tank containing the solid particles is generally in the shape of a rectangular prism or a cylinder. In practice, the geometry and dimensions should be selected in such a way to minimize the pressure losses and to maximize the mixing of particles. In Table 2, some bed dimensions and geometry studied numerically in the literature, are presented. In this study, a rectangular prism bed of which dimensions are 1 m of height, 0.28 m of width and 0.025 m of depth is considered. For multi-bed systems, rectangular prism beds can be placed in such a way that their lateral faces are contiguous to minimize the heat loss to the environment.

4.1.2. Solid Particle

In literature, various types of solid particles as both heat transfer fluid and thermal energy storage medium are investigated. Diago et al. [50] classified the desert sand samples taken from Abu Dhabi, Dubai, Al Ain and Liwa according to their thermal and optical properties. Baumann and Zunft [51] also investigated SiC , sintered bauxite, basalt, quartz sand (SiO_2), and normal corundum particles to be used in CSP applications. The important parameters in selection of solid particles are diameter and size distribution, bulk porosity, specific heat capacity, bulk conductivity, attrition and chemical composition. In this study, desert sand that is chemically composed of amorphous SiO_2 is used. The specific heat capacity of the particles is around 920 J/kgK at room temperature and 1130 J/kgK at 1000 K. There is almost linear relation between the temperature and specific heat capacity at the range of 300 - 1000 K [50]. Practically, determination of the thermal conductivity of the small particles in size of microns is a very hard process. For this reason, first, bulk thermal conductivity and bulk porosity of the samples are measured and by using these two parameters, particle thermal conductivity is calculated. Jund et al. [52] developed a classical molecular-dynamics model to predict the thermal conductivity of the vitreous SiO_2 particles and validated them with experimental results. The particle thermal conductivity is around 1 W/mK at room temperature, and nearly doubles at 1000 K.

The diameter of the monosized particles are specified as 275 micron with 2500 kg/m^3 of particle density. The bulk porosity is set to 0.4. Then, the particles can be classified as Geldart B type particles according to Figure 10.

4.1.3. Fluidizing Gas

In fluidized sand bed as direct contact heat exchanger, the fluidizing gas can also be used as the working fluid in power cycle as long as the particles carried over from the

bed are filtered. The main options for the gas are CO_2 to run a supercritical CO_2 - Brayton cycle and air to run air - Brayton cycle.

Table 2. Physical parameters used in various numerical studies in the literature

| | Particle | | Bed | |
| Author | Density | Mean Diameter | Geometry | Dimensions |
	kg/m^3	micron		m
Enwald et al. [53]	2600	700	Rectangular 2D	0.3x2.24
Peirano et al. [54]	2600	273	Rectangular 3D	0.8x0.7x0.12
Goldschmidt et al. [55]	2523	1500	Rectangular 2D	0.7x0.15
Wachem et al. [56]	2640	480	Axi-symmetric 2D	H=1.3 D=0.5
Halvorsen et al. [57]	2485	550	Rectangular 2D	19.5x63
Huilin et al. [58]	1600	1000 , 2500	Rectangular 2D	0.3x1
Gelderbloom et al. [59]	2100	200	Rectangular 2D	0.15x0.45
Syamlal et al. [30]	2650	117	Axi-symmetric 2D	H=2 D=0.229
Taghipour et al. [18]	2500	275	Rectangular 2D	0.28x1
Chiesa et al. [26]	2500	1000	Rectangular 2D	0.195x0.63
Lundberg et al. [60]	2485	154	Rectangular 2D	0.25x2
Vejahati et al. [19]	2500	275	Rectangular 2D	0.28x1.2
Hamzehei et al. [61]	2500	175,275,375	Axi-symmetric 2D	H=1 D=0.28
Deza et al. [62]	2600 , 1300	550 , 620	Axi-symmetric 2D	H=0.4 D=0.095
Duangkhamchan et al. [63]	2467	197	Half cone 3D	H=0.56 D=0.14 - 0.3
Battaglia et al. [64]	2000	428	Axi-symmetric 2D	H=0.7 D=0.0762
Krautz [65]	2500	275	Rectangular 2D	0.28x1
Asegehegn et al. [66]	2500	246	Rectangular 2D	0.32x1.2
Acosta-Iborra et al. [67]	2632	540	Cylindrical 3D	H=0.8 D=0.193
Hernández-Jiménez et al. [68]	2500	700	Rectangular 2D	0.5x2
Herzog et al. [69]	2500	275	Rectangular 2D	0.28x1
Li et al. [48]	2500	400	Rectangular 2D	0.25x0.75
Loha et al. [70]	2500	530	Rectangular 2D	0.155x0.4

Superheated steam as fluidizing gas should be avoided because moisture content may make particles sticky, which adversely affects the quality of fluidization. In this study, air is selected as the fluidizing gas. In Table 3, design parameters specified by user is presented.

Table 3. Physical model parameters

Bed width	0.28	m
Bed height	1	m
Static bed height	0.4	m
Particle density	2500	kg/m^3
Gas density	1.225	kg/m^3
Mean particle diameter	275	μm
Initial solids packing	0.6	-
Superficial gas velocity	0.11 , 0.21, 0.38 , 0.46	m/s
Minimum fluidization velocity [18]	0.065	m/s
Minimum fluidization bed height [18]	0.44	m
Air inlet temperature	300	K
Initial solid particle temperature	973	K

4.2. Numerical Solution Approach

The preferred solution algorithm to solve the governing equations for the flow field is pressure-based solver, which is suitable for incompressible subsonic flows. A pressure correction equation is derived from continuity and momentum equations in such a way that the velocity, corrected by pressure, satisfies the continuity [40]. Phase coupled SIMPLE (Semi-Implicit Method for Pressure-Linked Equations) algorithm, which is the extension of SIMPLE algorithm, is used for pressure-velocity coupling. The velocities for each phase are solved and coupled in a segregated fashion [71]. The procedure followed by numerical algorithm is represented in Figure 13. ANSYS Fluent 17.2, which is a commercial computational tool, is preferred due to its demonstrated capabilities to predict fluidization phenomena based on the Eulerian-Eulerian model [72].

4.2.1. Discretization Scheme

To discretize the computational domain spatially, first order upwind scheme is selected. Numerically, higher order discretizing schemes give more accurate results; however, these schemes require a lot of effort to converge to the solution. Various attempts were made to employ the higher order schemes, but trustable converged solution could not be achieved. Although the first order scheme creates high numerical diffusion errors, it gives accurate results at velocities near the fluidization [73][74].
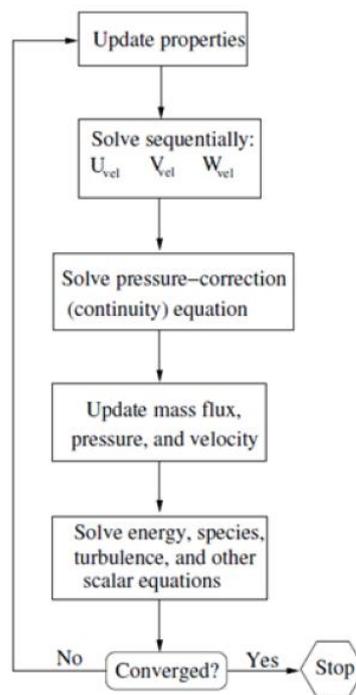

Figure 13. Pressure Based Segregated Algorithm [40]

For temporal discretization, implicit scheme is unconditionally stable compared to explicit scheme. Thanks to this advantage, larger time step for transient problems can

be selected; however, implicit scheme requires an iterative process and takes more time. In this study, first order implicit time discretization is preferred.

As a convergence criteria in each time step, the residuals for continuity and phase velocities are set to 10^{-5}, and maximum iteration is set to 30.

4.2.2. Mesh Refinement Study

Uniform and rectangular meshes are created by ANSYS Meshing tool. In Figure 14 computational domain with mesh sizes of 5 mm is visualized for both 2D model and 3D model. In the mesh refinement study, mesh size to particle diameter ratio is an important parameter.

Mesh sizes less than the ten times the particle diameter is strongly advised to obtain accurate results [25]. However, in the literature, meaningful results are obtained by setting this ratio to around 18 [75][54][19]. Taking account of the fact that reducing the mesh size by half ,which means quadrupling the number of cells in a 2D domain, brings along three times higher computational cost, a comparative study is considered necessary to determine the mesh size for the further simulations. To achieve grid independence in the computational domain, 5 mm x 5 mm and 2.5 mm x 2.5 mm uniform mesh arrangements are compared.

In Figure 15, it is shown that the bed height does not differ by mesh size significantly. Coarser meshes gives less fluctuating bed height at 1.2 s and 6 s, whereas finer meshes gives local peaks and dips. It may result from the fact that coarser ones could not predict solid cluster formation at upper part of the bed very well, which cause a biased prediction of the bed height.
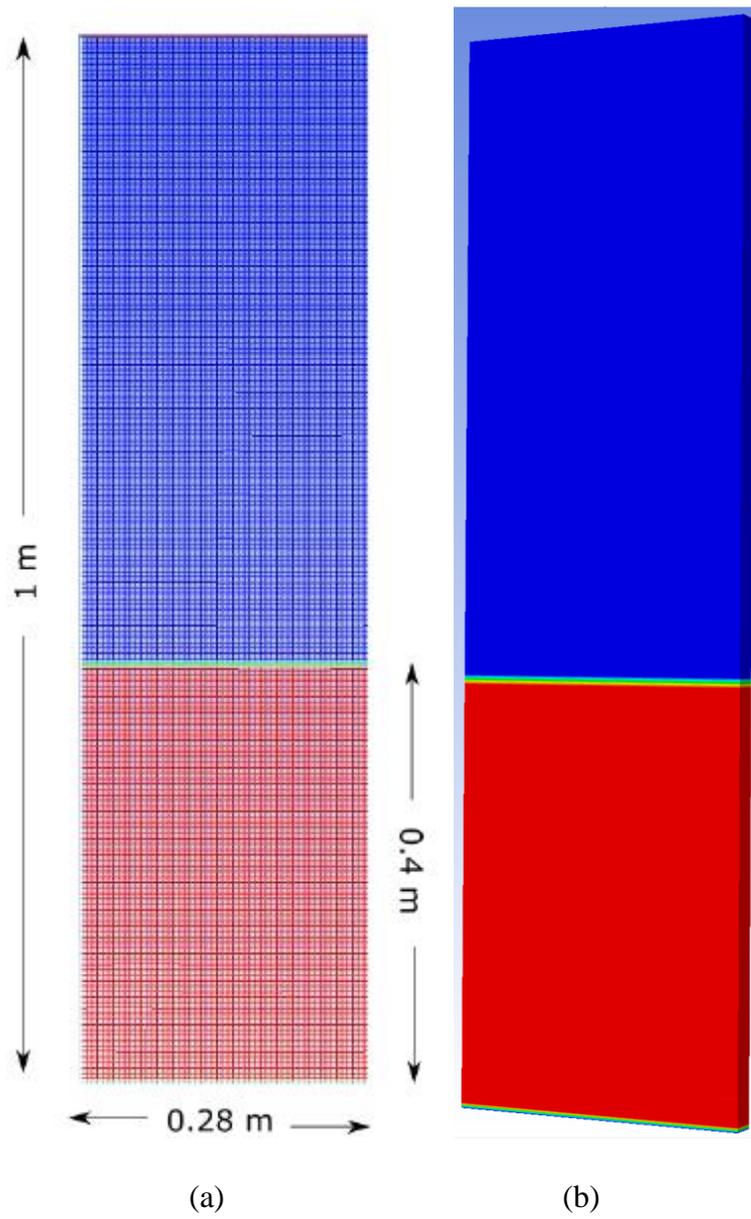
Figure 14. Mesh arrangement for computational domain (red color for initial solid
volume fraction of 0.6, blue color for the freeboard) (a) 2D model (b) 3D model
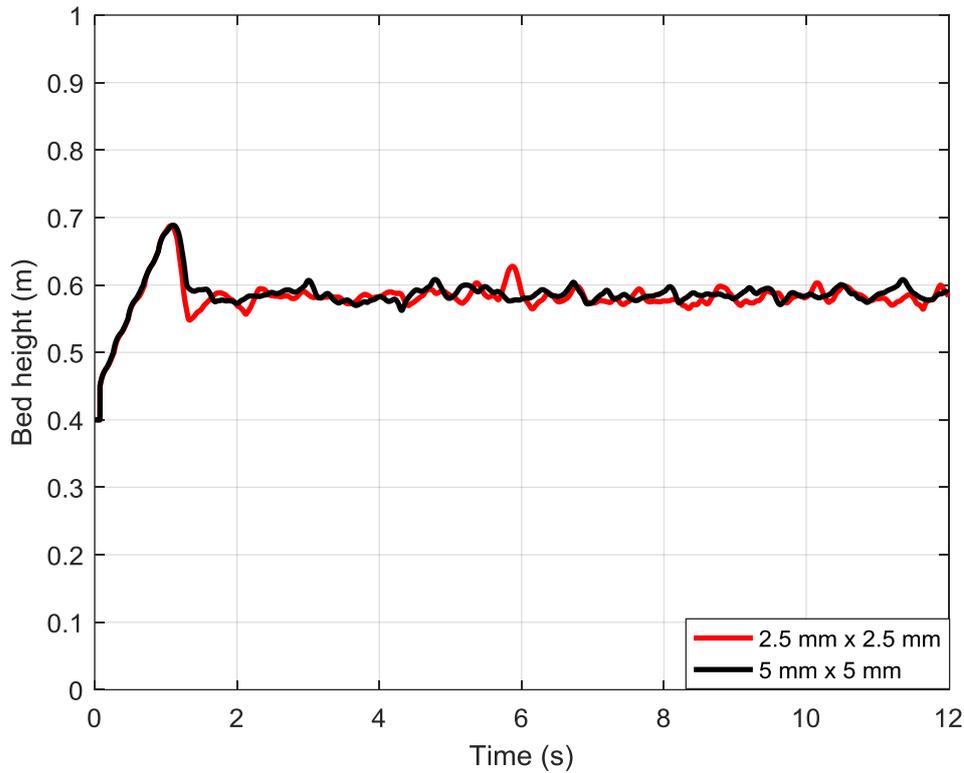
Figure 15. Bed height variation for different mesh sizes

Moreover, time averaged void fractions at height of 0.2 m from the bottom of the bed are compared in Figure 16, and no big difference is observed. It is concluded that grid independent results are achieved for 5 mm x 5 mm, so this mesh size is selected for the upcoming simulations

4.2.3. Time Step Optimization

The main limitation in selecting time step size is the convergence behavior of the numerical solution and computational power requirement. Small step sizes require too much computational effort whereas large step sizes result in high residual in flow variables. Note that beyond the time step size of 10^{-4} s, the residuals do not drop below

the specified values then, time steps of 10^{-4} s, 5×10^{-5} s and 10^{-5} s are selected for comparison study.
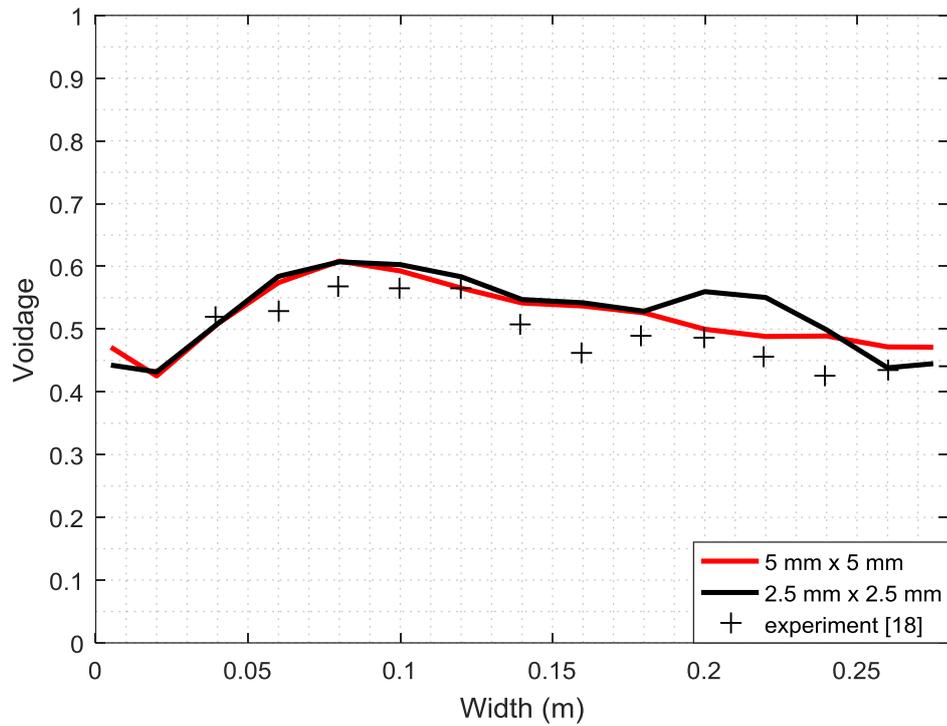
Figure 16. Comparison of time averaged voidage profile at z=0.2 m for different mesh sizes and experimental with experimental [18] results

Time step sizes are compared in terms of bed height and pressure drop across the bed. As seen in Figure 17 and Figure 18, until the bed reaches hydrodynamically steady state, all time steps give almost same results; however, for further seconds, although the peaks and dips do not match exactly, the time averaged values are same. Considering that a 1 second simulation with time step size of 10^{-5} takes approximately 3 days by using the available workstations, proceeding with larger step size, which is 10^{-4} s, makes a lot of sense.

43
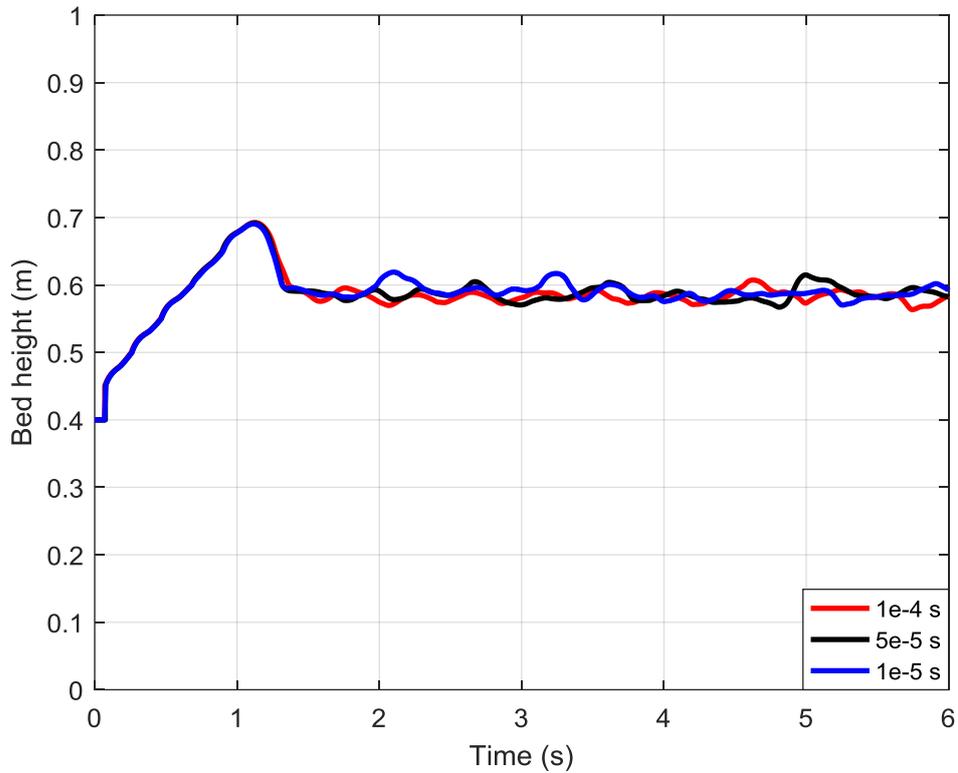
Figure 17. Temporal bed height variation for different time steps

4.2.4. 2D – 3D Comparison

In fluidization area, due to very high computational cost, 2D models are commonly preferred compared to 3D models in engineering scale applications. Although in the literature there is a consensus about the fact that 3D simulations give better predictions regarding statics and dynamics of the bed, pseudo-2D bed, in which the depth of the bed is so small that change in space and time averaged parameters along in that direction is negligible compared to the ones for other directions, can be modeled as 2D and successively employed for parametric analysis as long as it is validated with the 3D equivalent [76][54][66]. In this study, the bed geometry of which dimensions are

0.025 m x 0.28 m x 1 m, can be considered as pseudo- 2D bed due to its relatively small bed depth.
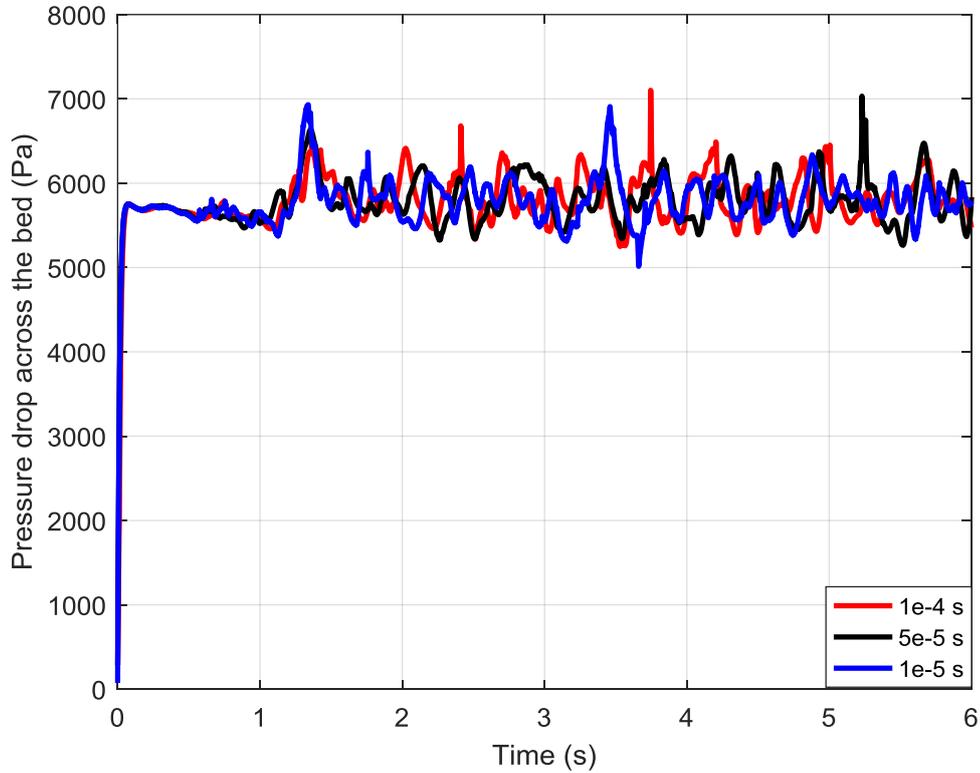
Figure 18. Temporal pressure drop variation across the bed for different time steps

The most noticeable disadvantage of using 2D model is the omission of the front and rear walls. This may result in poor estimation of bubbling rise velocity inside the bed [66]. From Table 4, it can be inferred that experimental bed height and pressure drop along the bed is comparable between 2D and 3D models.

Moreover, in Figure 19, it can be seen that the time averaged void fractions do not differ by dimensionality of the modeled bed significantly for moderate superficial velocity (0.38 m/s $\approx$ 5.8 U_{mf}). Although 2D model seems to better predict the experimental data quantitatively, 3D model better reflects the nature of the void

distribution because same boundary conditions are applied to walls, which must result in symmetry of void profiles around the mid of bed.

Table 4. Bed height and pressure drop comparison for 2D and 3D models

	Bed Height (m)			Pressure Drop (kPa)		
	mean	max	min	mean	max	min
2D	0.5858	0.6080	0.5623	5.815	6.646	5.208
3D	0.5729	0.5892	0.5523	5.777	6.401	5.382
Exp. [18]	0.5968	-	-	5.435	-	-

2D model could not predict the local dip at the middle of the bed whereas 3D model gives a local dip near the center, which also shown by experimental work.
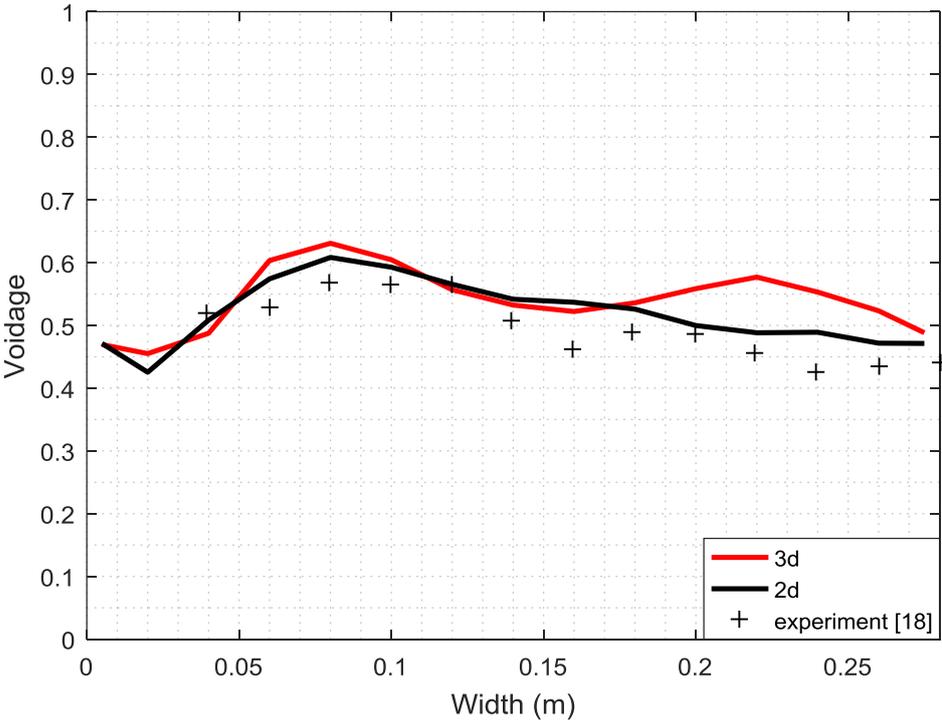
Figure 19. Comparison of time averaged voidage profile at z=0.2 m for 2D and 3D geometry with experimental [18] results (u_s=0.38 m/s)

In Figure 20, it can be observed that 2D model with mesh size of 2.5 m x 2.5 mm overpredicts the bed height slightly because the particles tend to stick to the walls in reality. However this discrepancy is not at the alarming rate and can be disregarded for the sake of less computational cost.

4.2.5. Time Averaging Study

In validation of bubbling beds, time and space averaged hydrodynamic parameters are preferably used rather than instantaneous results. Comparison between experimental and simulation results is difficult due to fluctuating behavior of the validation parameters.
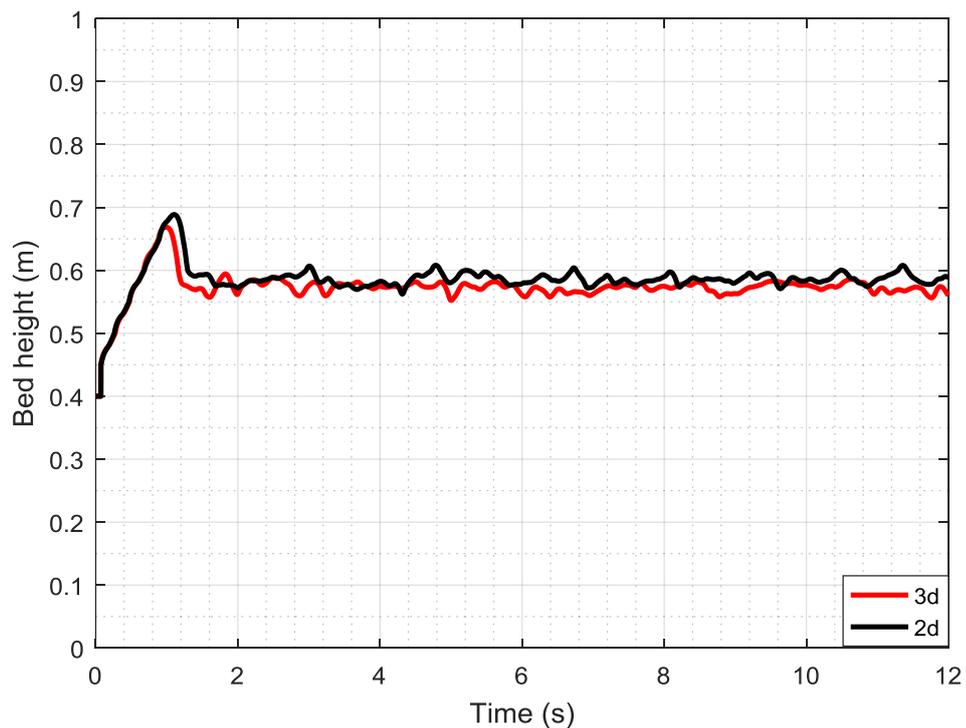
Figure 20. Bed height variation with time for 2D and 3D models

Interval for time averaging is determined in such a way that the initial time which is before the system reaches hydrodynamically steady- state, is disregarded. As seen in Table 5, there is no consensus about time averaging interval in the literature. In experimental studies, time averaging could be done by using first several hundred seconds; however, it is not feasible for numerical studies due to required high computational effort.

Mazzei et al. [77] predicts the steady state condition by observing bed height. First, bed height as a function of time is found as

$$h(t) = h_2 - (h_2 - h_1)exp\left(-\frac{u_2 - u_1}{h_2 - h_1}t\right)$$ (44)

where (u_1, h_1) is the initial equilibrium state and (u_2, h_2) is the final equilibrium state. The characteristic response time of the bed height, t_e, which is the time required to observe 95 % of the bed height increase ($h_2 - h_1$) is estimated as [77]

$$t_e = 3\tau \qquad ,where \quad \tau = \frac{h - h_{mf}}{u - u_{mf}}$$ (45)

Minimum fluidization condition (u_{mf}, h_{mf}) is chosen as initial state. Experimental study conducted by Taghipour et al. [18] is chosen as validation study. In that study, minimum fluidization velocity and minimum fluidization bed height are experimentally obtained as 0.065 m/s and 0.44 m, respectively. In Figure 21, bed height variation with time obtained numerically is compared with the one obtained with Equation (44) for different superficial velocities. The overshooting in first seconds mainly results from the unlocking of the bed at the onset of the fluidization. Most of the air cannot percolate through the bed due to insufficient air pressure at the bottom part and bed starts to rise.

However, this situation does not affect the steady state bed height, significantly. According to Equation (45), the bed reaches steady state at roughly 1.5 seconds for both 0.38 and 0.46 m/s of superficial velocity. For the sake of more accurate results, the simulation results of first three seconds are not taken into consideration. In order to decide the duration of the simulation time, air voidage profiles at a specified

elevation from the bottom of the bed are analyzed. To do so, air volume fractions are averaged for various time intervals, and each averaged value is compared with the previous time averaged volume fraction value.

Table 5. Interval for time averaging of hydrodynamic parameters in the literature

Author	Time Interval
Herzog et al. [69]	3-12 s
Taghipour et al. [18]	5-25 s
Loha et al. [78]	5-20 s
Vejahati et al. [19]	4-20 s
Zimmermann et al. [79]	10-20 s
Goldschmidt et al. [55]	2-20 s

The relative error for each time interval is presented in Table 6. Although low relative error means more accurate result, the computational cost increases as the time interval extended. Taking into account this trade-off, $3 - 12$ s of time interval is selected for time - averaging studies of hydrodynamic parameters. It should be noted that computational power requirement is the most decisive factor in optimizing of numerical model parameters. As a result of comparison studies done in Chapter 4, 2D computational model with uniform mesh size of 5 mm and time step size of 10^{-4} s is decided to be used for further simulations. Furthermore, it is concluded that hydrodynamic validation parameters are averaged in time interval of 3 - 12 s.
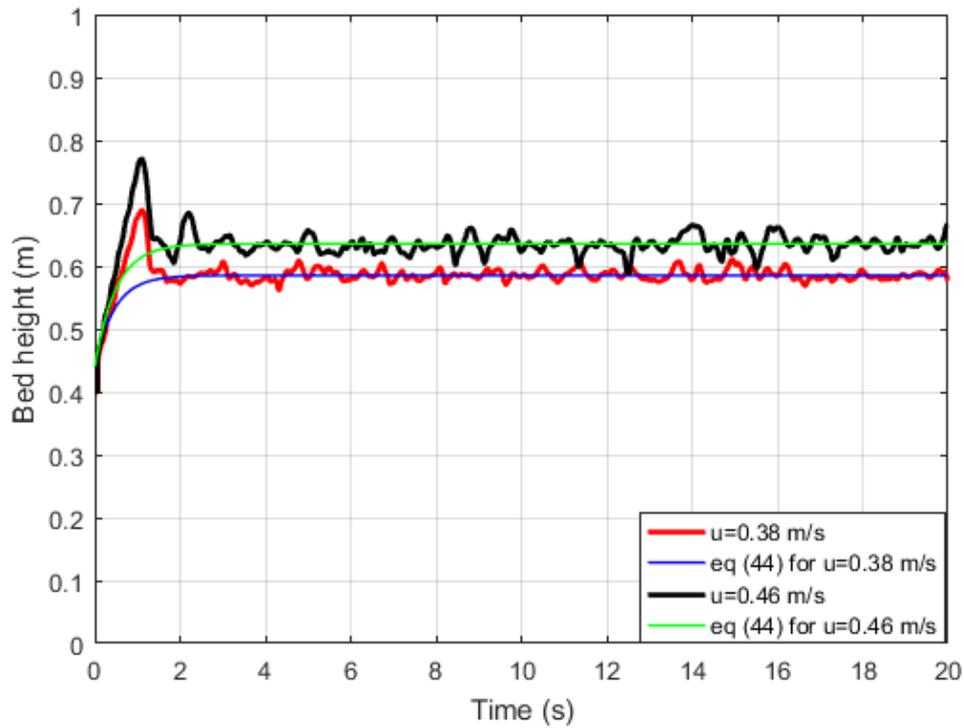
Figure 21. Comparison of simulation results and Equation (44) in terms of temporal bed height variation for U_s =0.38 m/s and U_s =0.46 m/s

Table 6. Parametric study to decide the time interval for averaging the parameters

Time interval	Relative error	Time interval	Relative error
3 - 4 s	5,185	3 - 14 s	0,154
3 - 5 s	3,021	3 - 15 s	0,116
3 - 6 s	1,529	3 - 16 s	0,101
3 - 7 s	0,920	3 - 17 s	0,100
3 - 8 s	0,658	3 - 18 s	0,100
3 - 9 s	0,395	3 - 19 s	0,112
3 - 10 s	0,358	3 - 20 s	0,131
3 - 11 s	0,475	3 - 21 s	0,128
3 - 12 s	0,258	3 - 22 s	0,104
3 - 13 s	0,166	3 - 23 s	0,087

CHAPTER 5

RESULTS AND DISCUSSION

5.1. Hydrodynamics Validation Results

Validation is defined as "the process of determining the degree to which a model is an accurate representation of the real world from the perspective of the intended uses of the model" [80]. In modelling of gas – solid multiphase flow, various approaches are employed to validate the hydrodynamical model. The prominent validation parameters are bubble shape and distribution, bed expansion ratio, bed height fluctuations, solids flow patterns, pressure drop across the bed, temporal voidage profiles and solids velocity distribution. In this study, quantitative validation studies are preferred rather than qualitative ones. For this purpose, temporal voidage profiles, bed expansion ratios and pressure drop across the bed are studied in detail.

5.1.1. Temporal Voidage Profile

Mathematical models that describe the fluidization phenomena are not mature yet. Some modelling parameters should be chosen properly to validate experimental data. In modelling of gas-solid suspensions in bubbling fluidized beds, restitution coefficient and specularity coefficient are the key parameters to accurately model particle - particle and particle - wall interactions. Li and Benyahia [48] compare variable and constant specularity coefficient approaches and state that overall effective specularity coefficient might be sufficient for modeling the tangential interaction between the solids flow and the wall. It is also stated that the specularity coefficient

fitted with certain experimental data may not work universally for the same system under different flow conditions.

Restitution coefficient also effects the bubble size and bubble rise velocity significantly. Goldschmidt et al. [55] state that hydrodynamics of dense gas fluidized beds (i.e. gas bubbles behavior) strongly depend on the amount of energy dissipated in particle-particle encounters. The pressure fluctuations depend on restitution coefficient. For this reason, a parametric analysis is conducted to decide the best values of specularity coefficient and restitution coefficient specifically for this study.

At a specified elevation from the bottom of the bed, volume fraction of the air is averaged by time. Porosity measurement is accepted as a sensitive test of the model since it is not prescribed as boundary condition inside the bed [42].

Percent relative difference between numerical data and experimental data [18] is calculated for each simulation. The calculation method is shown in Equation (46). y_{sim} and y_{exp} stand for simulation result and experimental result for void fraction, respectively whereas n is the total number of experimental observations.

$$\% \, Difference = \frac{\sum_1^n |y_{sim} - y_{exp}|}{\frac{n}{2}(y_{sim} + y_{exp})} * 100 \tag{46}$$

In Table 7, percent relative difference of simulations for various specularity and restitution coefficients are tabulated for Gidaspow drag model defined in Eq. (23) - (24), Syamlal O'Brien drag model defined in Eq. (12) - (17) and parameterized Syamlal O'Brien drag model defined in Eq. (12) - (22). It is seen that voidage profiles are not sensitive to restitution coefficient and specularity coefficient much; however, drag model affects this profile significantly. For parameterized Syamlal O'Brien drag model, there is almost no effect resulting from these model parameters. This may be due to the fact that the steady-state bed height is overestimated by parameterized model, which may result in more dilute flow in the bed. Then, particle − particle collisions become less important. As mentioned before, as specularity coefficient approaches to zero, particles tend to stick to the walls whereas it nears to one, walls

become slippier to particles. This ensures that void fraction decreases near the walls as specularity coefficient is lowered. As a result of parametric study, it is shown that low specularity values generally lead to voidage profiles to better match with the experimental data. Moreover, Li and Benyahia [48] studied on very similar bed geometry (0.25 m x 0.75 m) and concluded that effective specularity coefficient is 0.0746 as a result of several runs.

Table 7. Parametric Study to optimize specularity and restitution coefficient by using time averaged void profiles at z=0.2 m.

	0.38 m/s					0.46 m/s				
GIDASPOW										
Res. Coeff. / Spec. Coeff.	**0.7**	**0.8**	**0.9**	**0.95**	**0.99**	**0.7**	**0.8**	**0.9**	**0.95**	**0.99**
0.1	12,01	14,99	12,68	16,00	13,53	14,63	15,44	15,21	17,23	15,21
0.3	17,18	16,09	14,88	13,00	13,66	18,03	17,05	17,36	20,39	15,88
0.5	14,40	16,58	13,68	13,06	13,68	17,37	16,10	18,16	17,08	17,84
0.7	16,22	14,65	16,71	14,92	14,67	18,29	16,70	16,50	17,30	14,01
0.9	17,81	17,80	16,82	16,12	15,23	17,53	20,75	17,42	17,88	17,22
SYAMLAL O'BRIEN										
Res. Coeff. / Spec. Coeff.	**0.7**	**0.8**	**0.9**	**0.95**	**0.99**	**0.7**	**0.8**	**0.9**	**0.95**	**0.99**
0.1	12,16	10,92	12,62	13,18	6,18	14,90	13,31	15,87	15,45	12,26
0.3	12,77	10,35	11,66	12,51	9,20	14,82	12,84	13,76	14,00	12,33
0.5	13,12	12,93	12,51	11,07	10,13	22,71	15,13	18,79	16,24	12,54
0.7	11,72	10,47	12,92	11,32	12,36	16,44	15,95	17,71	15,17	14,50
0.9	13,22	10,60	12,59	12,69	9,60	13,84	13,36	15,38	18,27	17,29
SYAMLAL O'BRIEN PARA										
Res. Coeff. / Spec. Coeff.	**0.7**	**0.8**	**0.9**	**0.95**	**0.99**	**0.7**	**0.8**	**0.9**	**0.95**	**0.99**
0.1	32,82	33,20	34,32	35,90	37,27	35,12	35,39	37,48	39,30	39,65
0.3	32,51	32,51	33,76	36,57	34,69	35,77	36,10	38,49	39,61	37,58
0.5	32,96	35,35	37,84	33,87	34,01	34,52	37,52	38,37	37,32	40,21
0.7	34,72	32,82	34,76	35,98	37,02	35,77	37,32	39,54	38,65	39,93
0.9	33,29	34,42	36,57	38,21	37,37	35,83	37,04	39,09	39,46	38,24

In Table 7, it can be deducted that the simulations with restitution coefficient of 0.99 and specularity coefficient of 0.1 gives most accurate results in terms of voidage profile because percent relative errors for those parameters, which are highlighted, are relatively low compared other parameter couples. In Figure 22, it is seen that both Gidaspow and Syamlal O'Brien models gives similar results for superficial velocity of 0.38 m/s but they are like mirror image of each other. Syamlal O'Brien model predicts higher void fraction values at the left section of the bed whereas Gidaspow model gives higher values at the right section of the bed. The reason why particle intensity is high in one of the sides may be the fact that high air velocity in vertical direction create recirculation zones, which obstructs the particles to spread in lateral direction and particles tend to accumulate in one of sides. From Figure 23, one can conclude that both Syamlal O'Brien and Gidaspow models still predict void profiles fair enough in spite of increased superficial air velocity. Consequently, restitution coefficient of 0.99 and specularity coefficient of 0.1 is selected for the further simulations. Herzog et al. [69] also uses exactly same geometry and particles by using Multiphase Flow with Interphase Exchanges (MFIX), which is an open source code, to model the bubbling beds. It is concluded that MFIX also predicts the void distribution fairly well except the center of the bed.

5.1.2. Bed Expansion Ratio

The maximum bed height (H) is the elevation at which the solid – gas mixture rises at most, when the system reaches steady-state hydrodynamically. Bed expansion ratio is the ratio of the bed height expansion ($H - H_0$) to static bed height (H_0). Numerically, to decide how much the amount of bed expansion is, is not straightforward. At high superficial velocities, the upper region of the bed is so dilute that it results in biased prediction of the bed height.
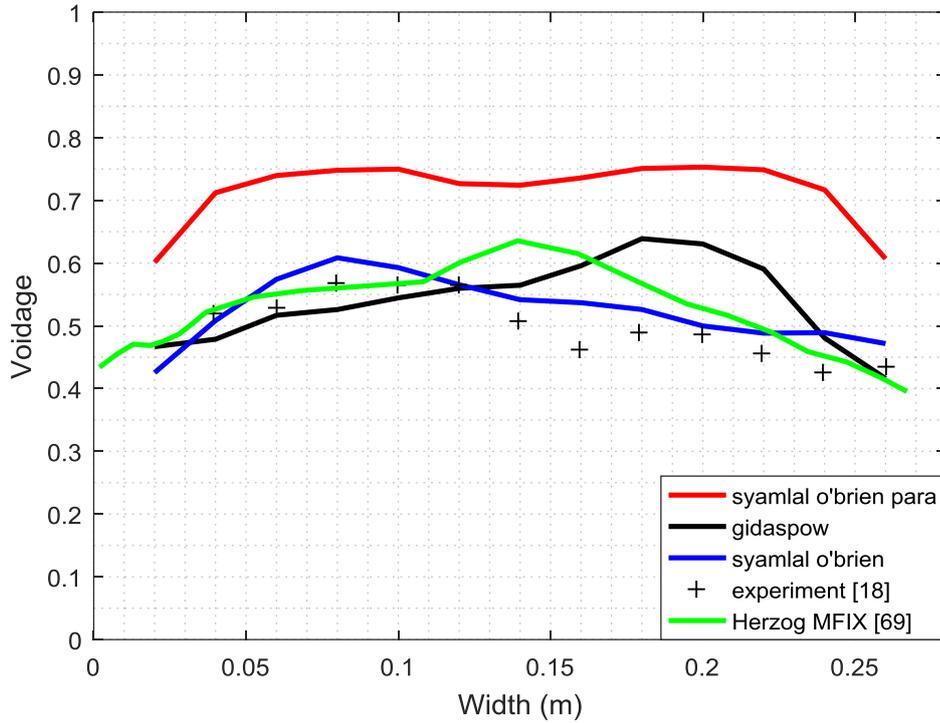
Figure 22. Comparison of drag models for spec. coeff. =0.1 and res. coeff. =0.99 and u_s=0.38 m/s at z=0.2 m with the experimental and numerical studies

Vejahati et al. [19] proposed that the elevation containing 95% of the bed weight can be considered as the expanded bed height.

$$\% \ Bed \ Expansion \ Ratio = \left(\frac{H - H_0}{H_0}\right) * 100 \tag{47}$$

In Figure 24, it can be deduced that Gidaspow drag model is in excellent agreement with the experimental data whereas small deviations are observed for Syamlal O'Brien model. This is mainly due to the fact that even for air velocity of 0.11 m/s, Syamlal O'Brien model could not predict fluidization, which results in zero bed expansion ratio.
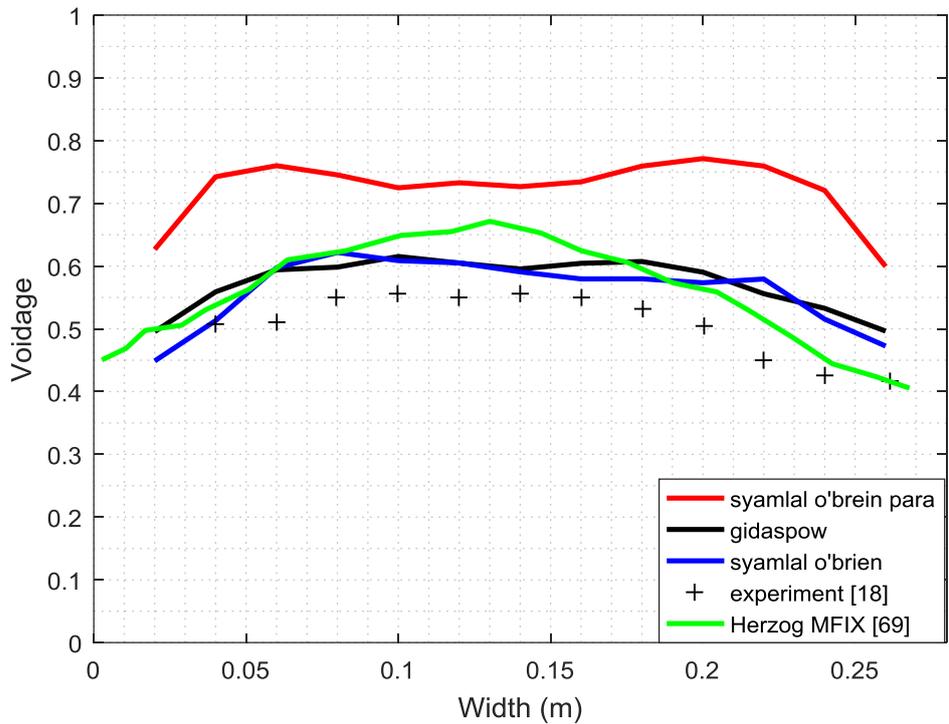
Figure 23. Comparison of drag models for spec. coeff. =0.1 and res. coeff. =0.99 and u=0.46 m/s at z=0.2 m with the experimental and numerical studies

Parameterized Syamlal O'Brien model highly overpredicts the bed expansion. Herzog et al. [69] also found similar results by using Syamlal O'Brien drag model at low superficial velocities; however, MFIX gives overpredicted bed expansion ratio for high superficial velocities. Note that to check the repeatability of the results, all simulations are run three times and it is observed that the time averaged bed expansion ratio does not change by more than 1 %. In Appendix A, evolution of bed height with time is presented for all drag formulas.
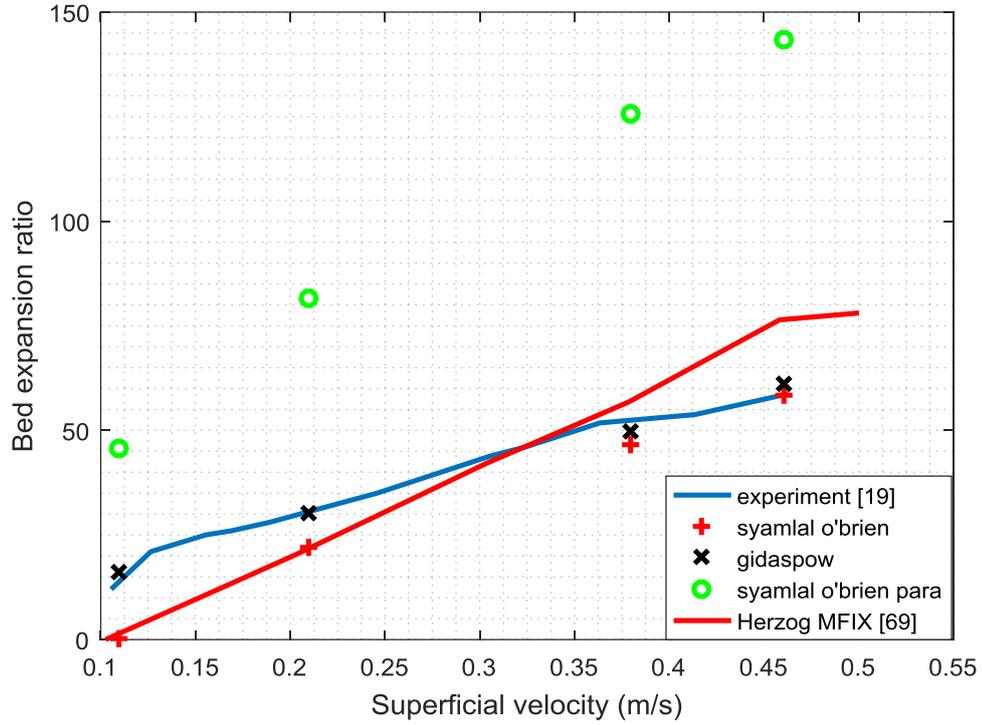
Figure 24. Bed Expansion ratio for various drag models and superficial velocity and comparison with the experimental and numerical studies

5.1.3. Pressure Drop

Theoretically, air pressure drop across the bed increases as superficial velocity increases until the onset of the fluidization, as seen in Figure 25. Once the bed starts to fluidize, the bed pressure drop remains constant. The weight of particles is simply the multiplication of the pressure drop and bed bottom area, if pressure drop due to the wall interaction is neglected. At minimum fluidization condition, the air pressure drop is theoretically calculated as [20]

$$\frac{\Delta P_b}{L_{mf}} = (1 - \epsilon_{mf})(\rho_s - \rho_g)g \tag{48}$$

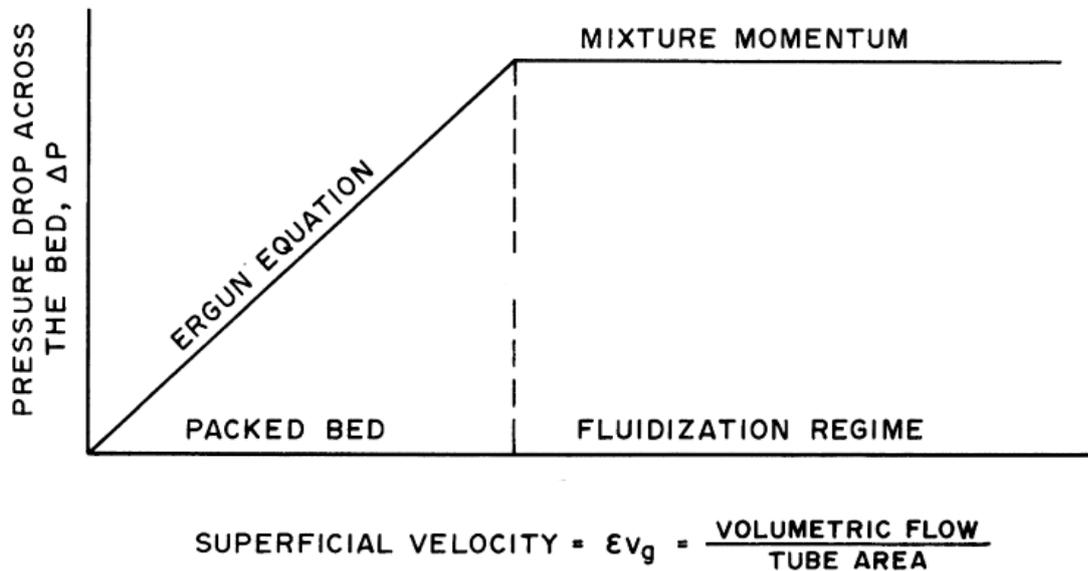where L_{mf} is the bed height at minimum fluidization condition.

Figure 25. Theoretical pressure drop across the bed as a function of superficial velocity [42]

Taghipour et al. [18] reported experimental minimum fluidization bed height and voidage as 0.44 m and 0.5, respectively. In Figure 26, experimental and theoretical trends are compared with drag model results. It can be clearly seen that at moderate velocities (0.21 m/s and 0.38 m/s) all drag models predict similar bed pressure drop. However, at low velocity (0.11 m/s), Syamlal O'Brien model underpredicts the pressure drop because fluidization has still not been observed although experimental minimum fluidization velocity was exceeded. In Figure 27 and Figure 28, computationally found pressure difference between different elevations inside the bed are compared with experimental data. The reason why parameterized Syamlal O'Brien models could not predict pressure differences accurately at higher velocities is that more particles are found to be located above the pressure transducers locations in the experiment, which results in overestimated bed expansion. Then, some portion of air

58

pressure is still available to balance the weight of the of particle clusters above. It can be deduced that Syamlal O'Brien model better predicts the pressure distribution across the bed although at low velocities.
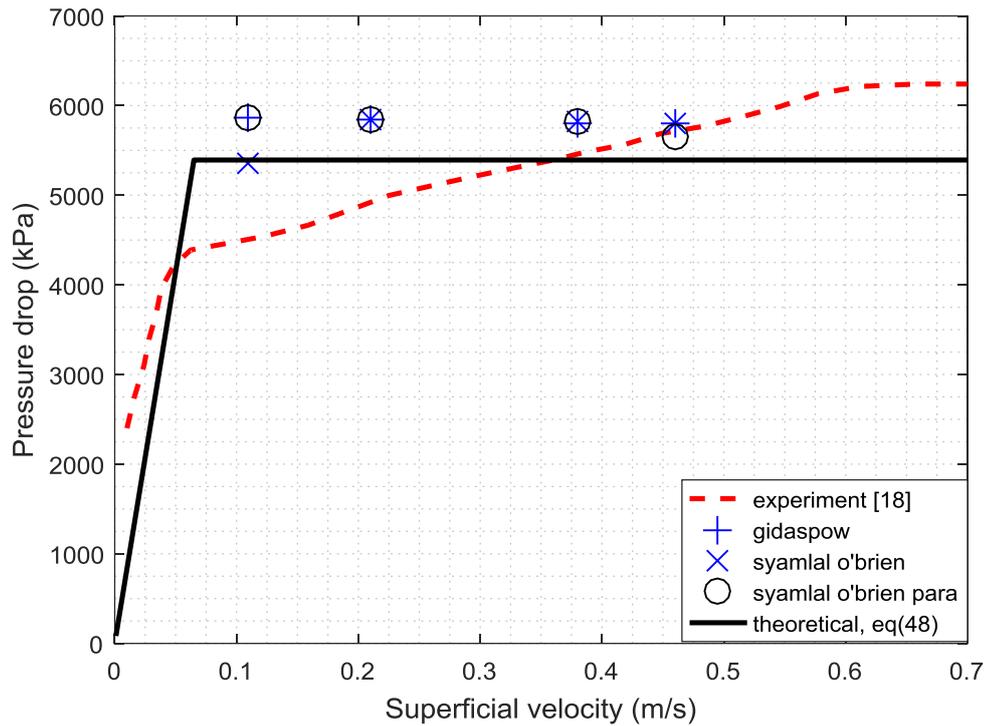

Figure 26. Pressure drop across the bed for different drag models

As a result of various attempts to optimize hydrodynamics parameters, Syamlal O'Brien drag model with 0.99 of restitution coefficient and 0.1 of specularity coefficient is chosen as the best case.
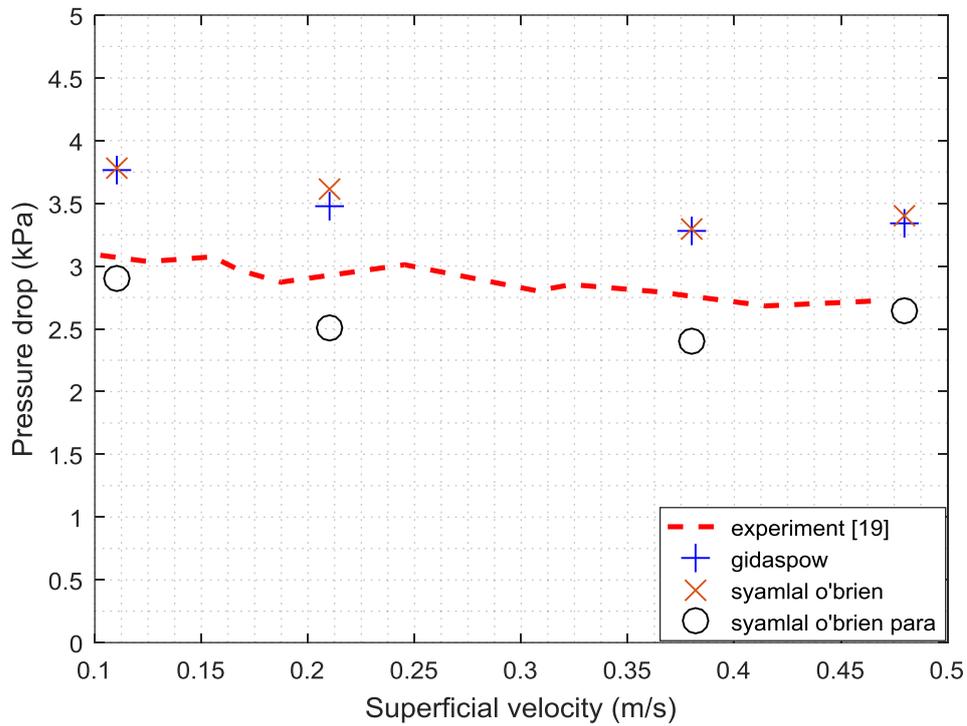
Figure 27. Pressure drop inside the bed ($P_{z=0.03\ m} - P_{z=0.3\ m}$)

5.2. Thermal Results

As stated earlier, the main intended use of the bubbling bed is to obtain high temperature air by recovering heat from hot solid particles to operate a thermodynamic cycle during the night time. For this purpose, first, the bed is modeled and validated hydrodynamically.
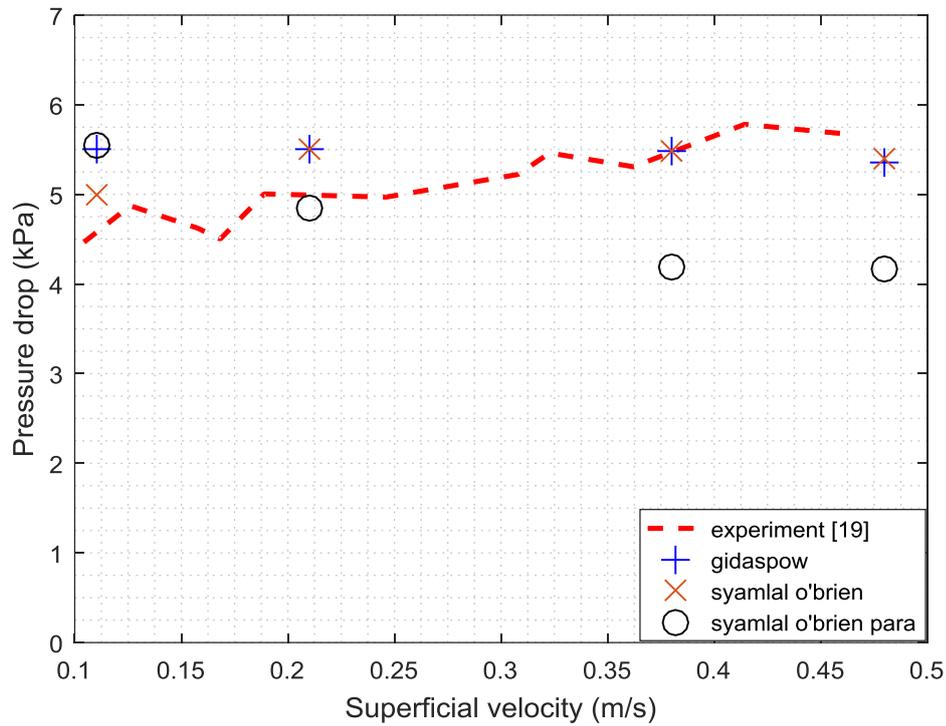
Figure 28. Pressure drop inside the bed ($P_{z=0.03\ m} - P_{z=0.6\ m}$)

In thermal modelling, particle thermal conductivity and bulk specific heat capacity are modeled as temperature dependent. Taking account of the fact that the mass of the air inside the bulk is negligible compared to mass of the particles, bulk specific heat capacity is assumed to be equal to particle specific heat capacity. Air thermal properties are modelled as temperature-dependent, too. The walls are considered as well-insulated, so no heat exchange between the walls and bulk is modelled. The walls are assumed to be very thin so, the thermal mass is negligible. In results, it is observed that there is no considerable solid temperature gradient, i.e. not more than 1°C temperature difference between the particles with maximum and minimum temperature, inside the bed, which is a well-known characteristic of bubbling bed.

5.2.1. Interphase heat transfer coefficient

Interphase convective heat transfer coefficient (h) for superficial velocities of 0.38 m/s and 0.46 m/s at different elevations are plotted in Figure 29. Except for first several seconds, results for both velocities show that there is almost linear relation between interphase heat transfer coefficient and time. As shown in Equation (42) and (43), h is function of gas thermal conductivity, air Prandtl number, particle Reynolds number and solid volume fraction. Considering the temperature dependency of Re_s and Pr is so weak, gas thermal conductivity has a greater effect on interphase heat transfer coefficient. Because gas thermal conductivity increases almost linearly with temperature, linear decrease in heat transfer coefficient is not surprising according to Equation (43). As seen in Figure 29, as elevation increases, heat transfer coefficient decreases. This may due to the fact that as solid volume fraction increases, the velocity of the interstitial gas increases and it results in a decrease Re_s. Both increasing ε_s and decreasing Re_s lead to lower Nu as elevation increases. In Figure 29, numerically found h values are averaged every 5 seconds to show the trend of the mean values. However, in reality, h has an oscillating behavior as presented in Figure 30. This is mainly due to continuous bubble interactions in the bed. Instantaneous void fraction variations dramatically affect the effective thermal conductivity of gas-solid suspension, which results in continuous fluctuations in heat transfer coefficient. It can be also noted that as superficial velocity increases, heat transfer coefficient decreases more rapidly.

Lungu et al. [81] investigated interphase heat transfer coefficient in bubbling beds and found it as 94.22 W/m^2K by considering a fluidizing gas with thermal conductivity of 0.00257 W/mK, which is one tenth of the one used in this study at nearly room temperature. Although they used particles with different density and diameter, Nusselt number is found to be 12.75 at nearly room temperature for superficial velocity of 0.44 m/s. In this study, space averaged Nusselt number is found as 11.66 at room temperature for superficial velocity of 0.46 m/s, which is quite comparable with Lungu et al. [81] results.
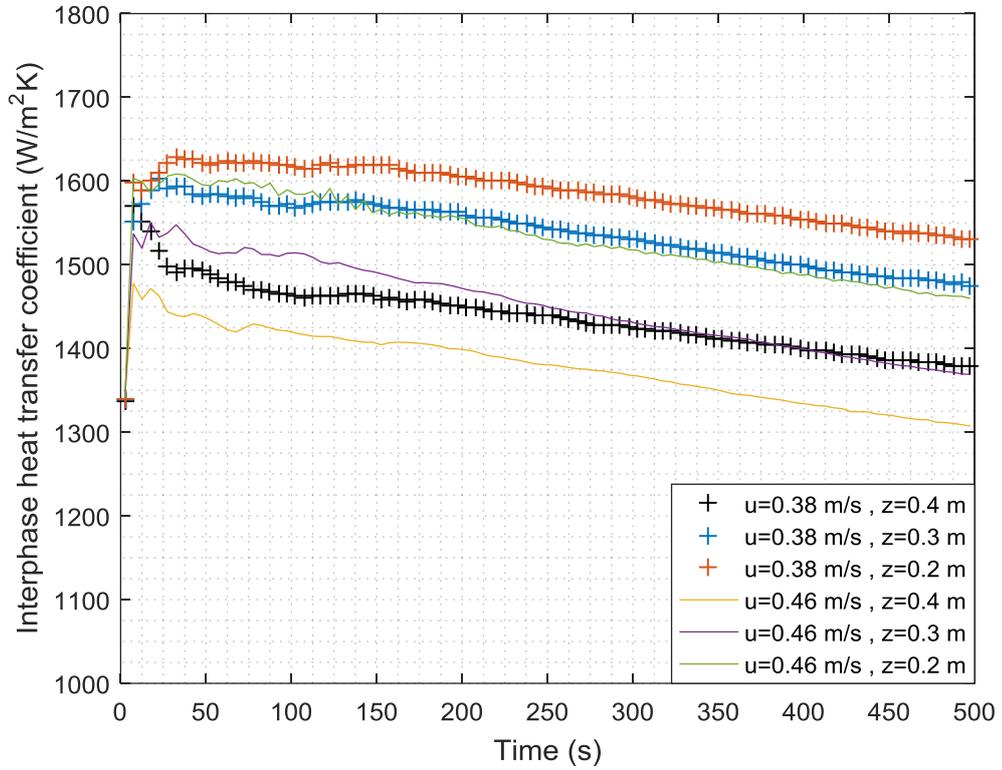
Figure 29. Interphase heat transfer coefficient variation with time for various elevation from the bottom of the bed

In Figure 31, interphase heat transfer coefficient variation with respect to bed temperature is plotted. It is observed that this coefficient varies with bed temperature, superficial velocity and elevation. Almost linear relation is observed as from 940 K. Linear regression can be applied to express interphase heat transfer coefficient as a function of bed temperature, which is as follows
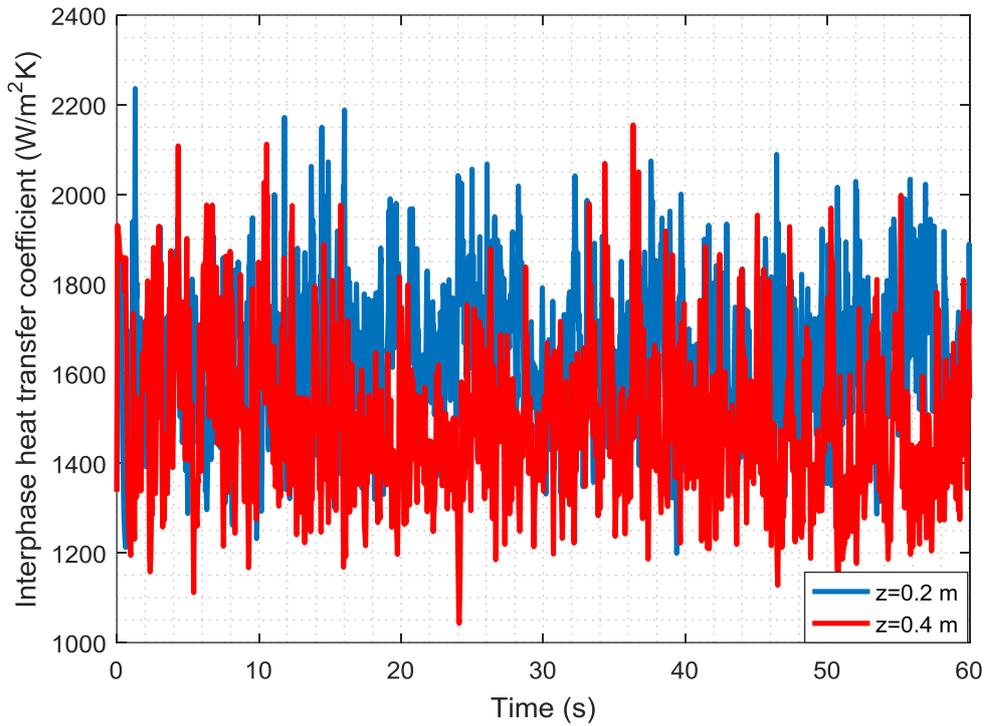
$$h(T) = aT+b \tag{49}$$

Figure 30. Time oscillating behavior of interphase heat transfer coefficient

$(u_s=0.38$ m/s)

In Table 8, coefficient of linear fit and R-squared values for each velocity – elevation is tabulated.

Table 8. Coefficients of linear fit of interphase heat transfer coefficient as a function of bed temperature

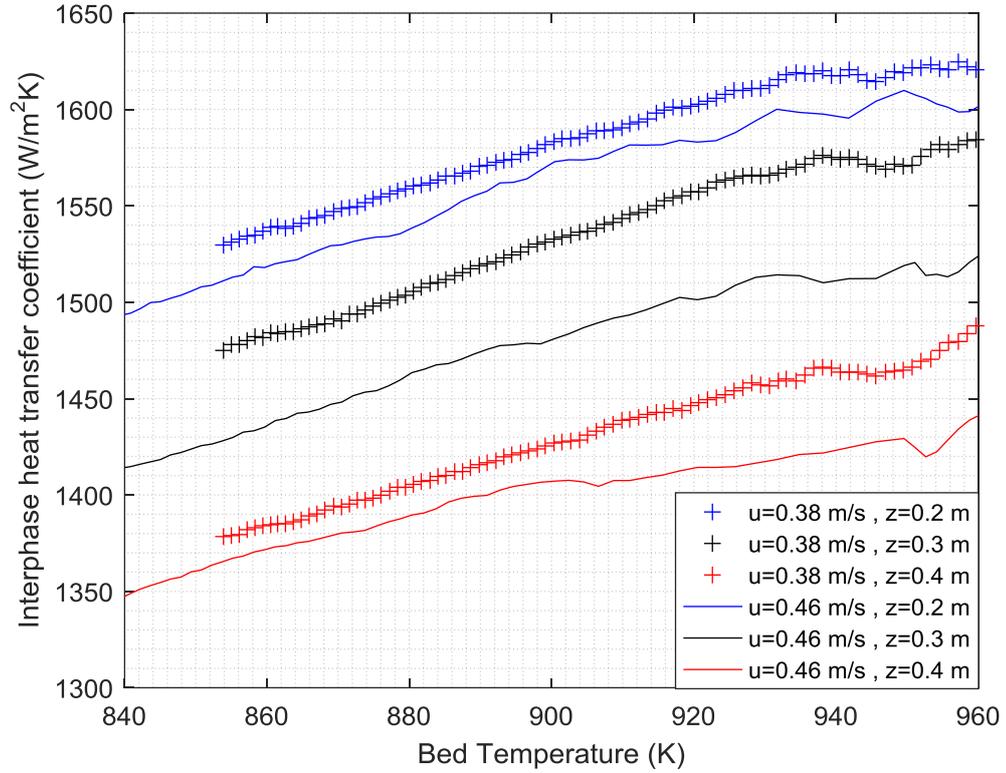|	z	a	b	R^2
0.38 m/s	0.2	1.028	654.347	0.987
	0.3	1.227	425.932	0.996
	0.4	1.058	473.72	0.998
0.46 m/s	0.2	1.155	523.682	0.993
	0.3	1.117	474.428	0.993
	0.4	0.892	598.067	0.972

Figure 31. Interphase heat transfer coefficient variation with bed temperature for various elevation from the bottom of the bed

5.2.2. Temperature variation of sand and air with time

According to obtained results, the air temperature rises to particle temperature instantly when phases interact with each other. It means that the convective thermal resistance between phases is so low that even a small residence time is enough for heat transfer. Van Heerden et al. [82] states that the relaxation time, τ_g , needed to establish a steady temperature gradient inside a fluidized bed can be calculated as

$$\tau_g = \frac{2.3\rho_g C_{p,g} d_s^2}{36 k_g} \tag{50}$$

Required relaxation time as a function of particle temperature is plotted in Figure 32. For superficial velocity of 0.38 m/s, the required elevation to obtain steady temperature gradient is around 0.0418 mm from the bed. This amount of height cannot be captured with 5 mm size meshes, but it can be qualitatively stated that air temperature instantly rises near the solid temperature after the very first cell at the bottom.
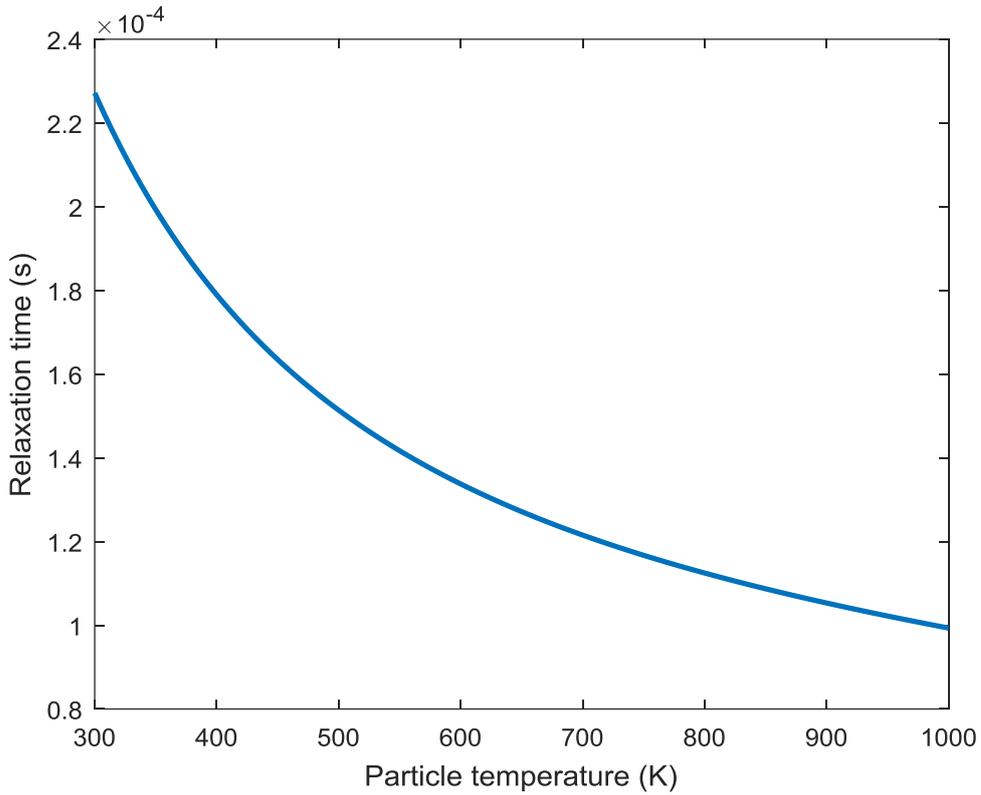

Figure 32. Required time to establish steady temperature gradient inside the bed as a function of particle temperature

In Figure 33, temperature variation of bulk solid and air exit with time is presented. Small fluctuations in air exit temperature result from continuous bubble formation inside bed. Consequently, it can be assumed that a single temperature is shared by phases by neglecting temperature gradients. In Figure 34 elapsed time to reach the bed to dead state temperature of 300 K is presented for two different operating velocities. First 500 seconds are simulated and the remaining part is extrapolated exponentially.

The mathematical explanation of why an exponential fit is employed can be shown if energy balance for a lumped body is derived.

$$mC_p \frac{dT_s}{dt} = -hA(T_s - T_{air}) \qquad (51)$$

where T_s is the instantaneous lumped body temperature. Let $T=T_s-T_{air}$ and rearranging Equation (51) yields

$$\frac{dT}{T} = -\frac{hA}{mC_p} dt \qquad (52)$$

If h and C_p are assumed to be constant, integration results in

$$T = C_1 e^{\left(-\frac{hA}{mC_p}\right)t} \qquad (53)$$

$$T_s = C_1 e^{\left(-\frac{hA}{mC_p}\right)t} + T_{air} \qquad (54)$$

If h and C_p are modeled as temperature dependent, it makes C_1 temperature dependent but does not change the exponential decay behavior of temperature with time.

As seen in Figure 34, regardless of superficial velocity, the temperature of the bed drops to 300 K in around 5000 s. However, increasing superficial velocity leads to more rapid run out of the bed because the air thermal energy at dead state is not useful energy. Practically, extracting thermal energy from particles until the bed reaches the dead state temperature of 300 K does not make sense because to obtain high turbine efficiency, air exit temperature from the bed should be maximized. However, as time passes, air exit temperature decreases exponentially, as shown in Figure 34. Then, a lifetime is defined for a single bed. The lifetime is the amount of the time required for the bed to reach a specific cold silo temperature, which is a design parameter. For example, if air exit temperature of 600 K or above is needed to run the turbine, the lifetime of the bed is 800 s for $U_s = 0.46$ m/s and 1000 s for $U_s = 0.38$ m/s.

Relatively cold particles (<600 K) is reheated at riser to be used later. It should be noted that hydrodynamics limitations should not be disregarded since increasing superficial velocity to obtain higher air flow rates results in fluidization regime change.
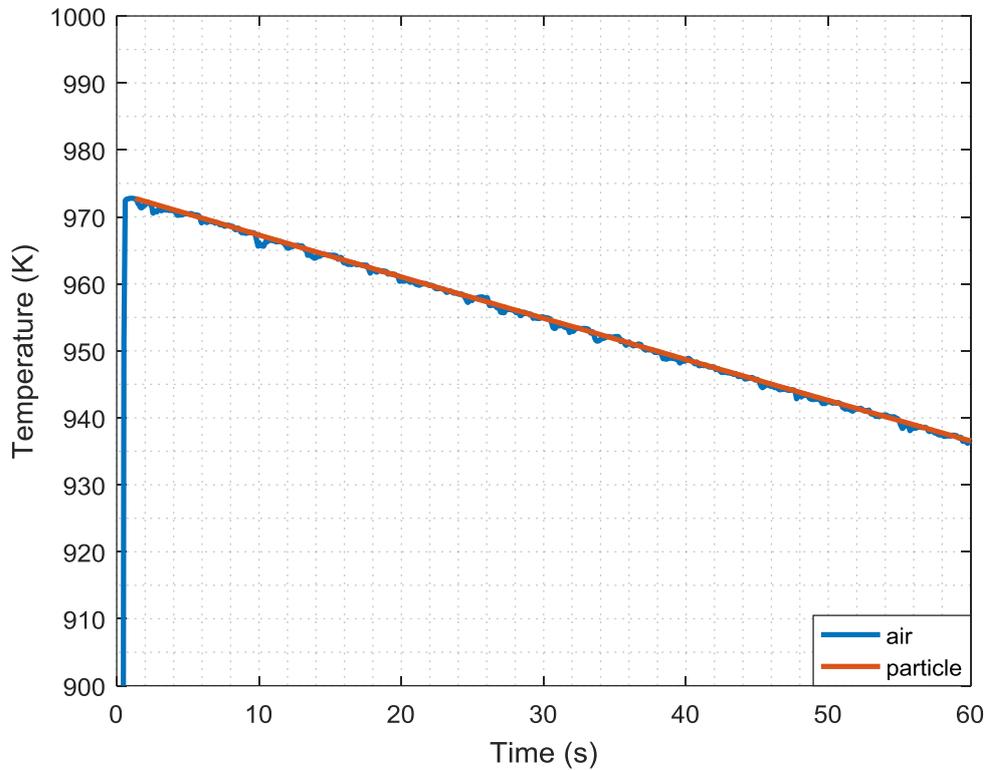
Figure 33. Temporal temperature variation of sand and air for first 60 s

5.2.3. Preliminary System Modelling and a What-If Analysis for Ivanpah

After determining the thermal behavior of a single bed, one can use the obtained thermal results to model a larger scale TES systems. To show the feasibility of the bubbling fluidized sand bed as a storage system, many of the beds are used to construct a TES system for Ivanpah Solar Power Plant, which has net nameplate capacity of 377 MW and capacity factor of 0.314 [8]. It can be calculated the required number of beds to achieve a thermal storage for an equivalent of Ivanpah Solar Power Plant so that electricity can be provided for the night time. Ivanpah average daily produced thermal power is calculated as 9978 MWh-thermal. It can be roughly estimated that half of this amount is stored for night time. The considered data for Ivanpah is given in Table 9.
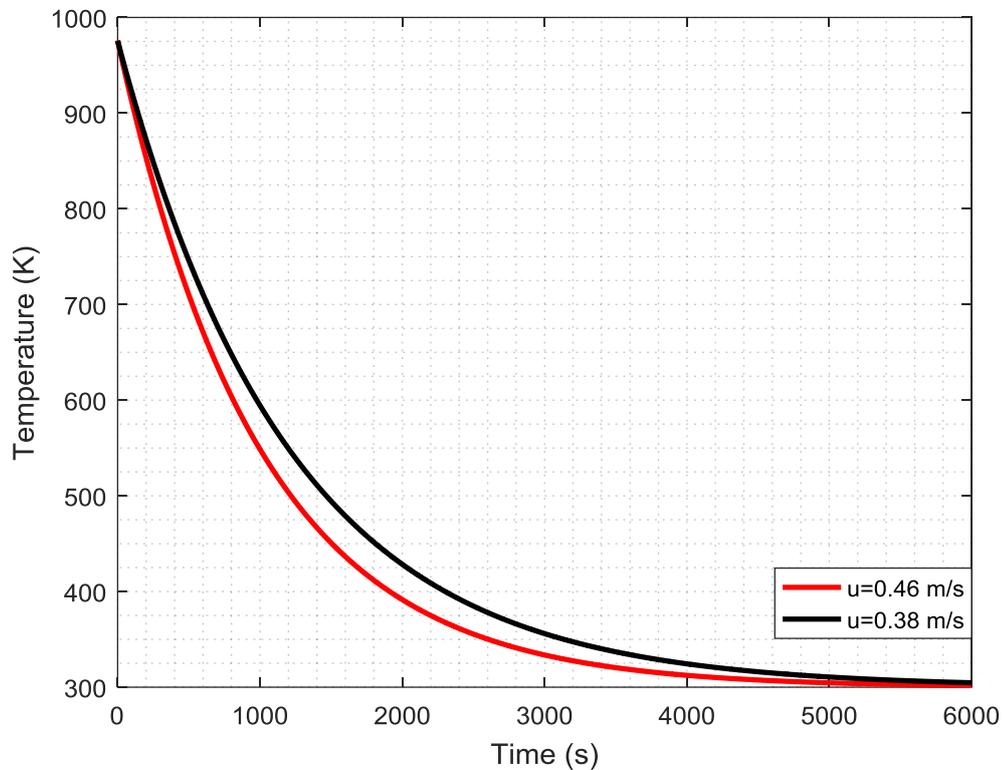
68

Figure 34. Temporal bed temperature variation for different superficial velocities

To minimize the heat loss to the ground, beds should be placed circularly so that a big circular disk including more than 6 million beds is created, which is practically challenging. Total upper area of beds (0.025 m x 0.4 m x 6262844) is used to find the hydraulic diameter. This leads to a circular disk with dimensions of 236 m diameter and 1 m depth, which is placed into ground. Heat loss is calculated by only considering the conduction from the bottom of the circular disk to the soil, which can be assumed as a semi-infinite medium.

Table 9. Ivanpah Thermal Storage Unit in numbers

Total Annual Thermal Power	3,641,946	MWh-thermal
Average daily thermal power	9,978	MWh-thermal
Night Time	12	hour
Daily storage capacity	4,989	MWh
Required number of bed	6,262,844	-
Hydraulic diameter (D)	236	m
Shape Factor (S)	473	m
Conductivity of soil (k_{soil})	0.3	W/mK
Soil Temperature	287	K
Average bed temp	637	K
Thickness of airbox (L_{air})	0.1	m

Since the diameter of the bed is very big compared to thickness of the bed, it is assumed that heat loss is only from the bottom to the soil. For this geometry, conduction shape factor (S) is two times of hydraulic diameter (D) of thermal energy storage system [83]. There are also air inlets with manifolds (airboxes) at the bottom between the stored sand and soil. Both of semi-infinite medium and manifold creates conductive thermal resistances. The sum of conductive resistances gives the total thermal resistance as

$$R_{tot} = \frac{1}{S\,k_{soil}} + \frac{4L_{air}}{k_{air}\pi D^2} \tag{55}$$

Total heat loss is the function of sand temperature in the bed. All other parameters are assumed to be constant and the total heat loss is calculated from

$$Q_{loss} = \frac{T_{sand} - T_{soil}}{R_{tot}} \tag{56}$$

To produce electricity from hot air, Closed Brayton cycle is proposed. The representative figure of Brayton cycle is shown in Figure 35. First, the fresh air (state 1) at 300 K enters

the TES system and is heated up through heat recovery from hot solid particles. Hot air (state 2) of which temperature is design parameter enters the turbine to produce electricity for the night time. With the help of cooler and compressor, thermodynamic cycle is completed. The polytropic index for turbine and compressor is selected as 1.3. The pressure drop in TES is found as 5.812 kPa from hydrodynamics model for 0.38 m/s of superficial air velocity whereas cooler is assumed to be isobaric.
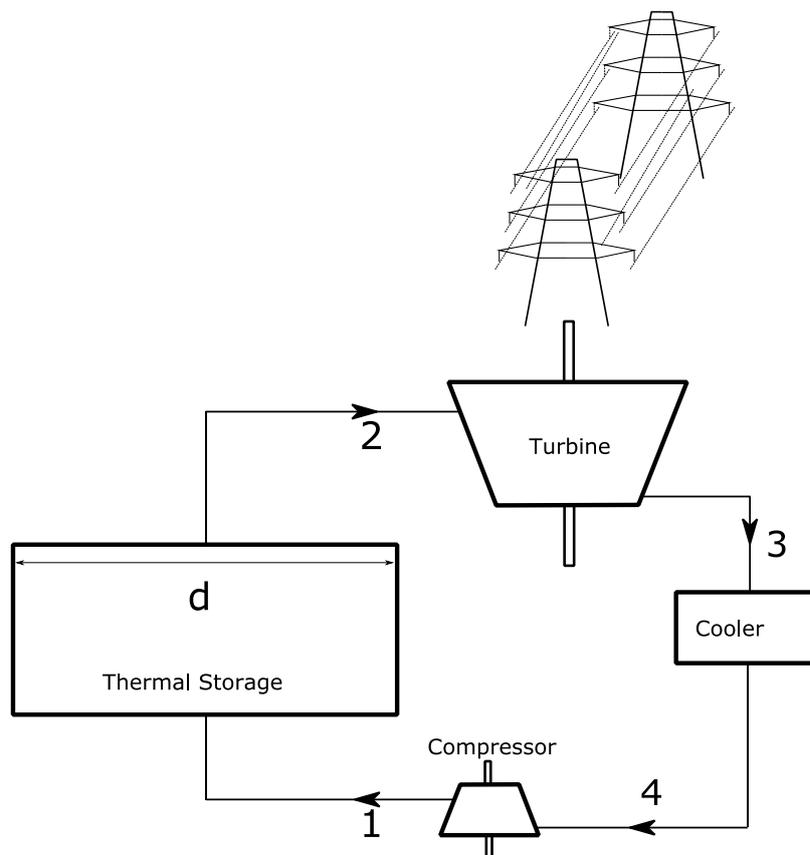

Figure 35. Closed Brayton Cycle for TES system

It is predicted that a single bed reaches to dead state temperature (300 K) in 5000 s or ~ 83 min from Figure 34. It is clear that recovering heat from bed during 83 min is not possible because as turbine inlet temperature decreases, a decrease in turbine efficiency is expected. At this point, average air exit temperature should be defined for turbine inlet.

An approach to determine the required number of active beds to keep the exit temperature constant is developed. In this approach, while a number of fresh beds is constantly activated, an equal number of beds that reaches to relatively low temperatures is deactivated so that the number of active beds does not change with time. Although the process seems to be transient for a single bed, it can be regarded as steady-state for the whole system. Determination of air-exit temperature, the air mass flow rate and lifetime (active discharge time) of a single bed in the storage system is handled as an optimization problem.

In Figure 36, it is shown that as the required air mass flow rate to keep the turbine inlet temperature constant increases, the net power production increases to a certain extent. At this point, since air exit temperature decreases significantly, turbine efficiency dominates the net power production.
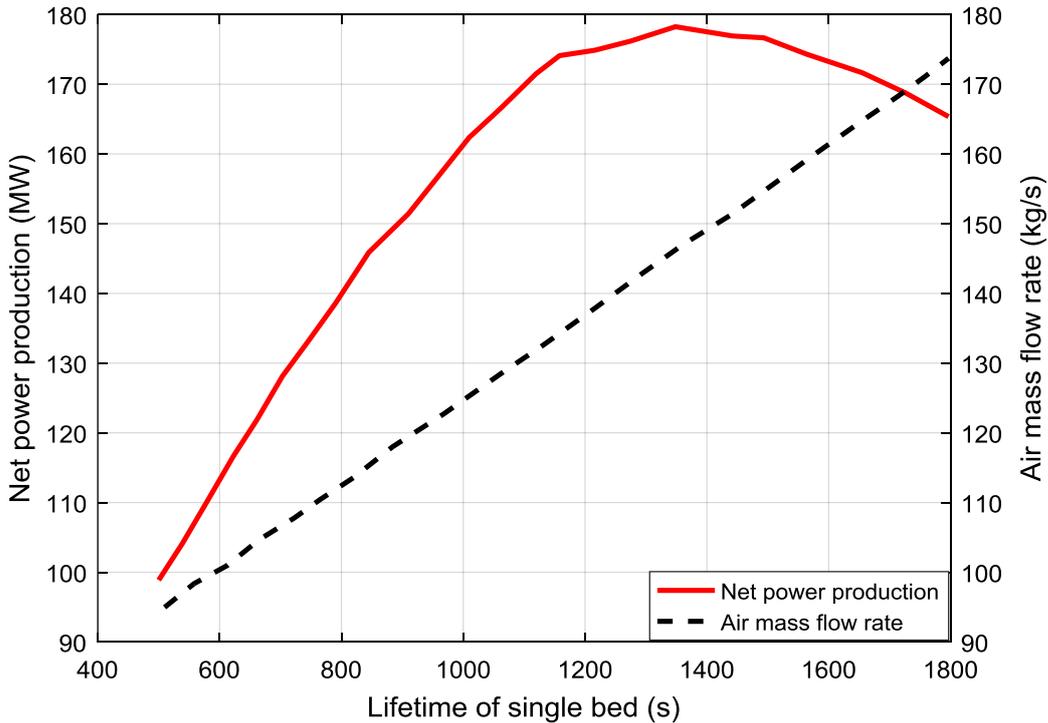

Figure 36. Net power production of TES system and required air mass flow rate with respect to lifetime of a single bed

In Figure 37, the relation between turbine inlet temperature and net power produced per unit air mass flow rate is presented. Since turbine efficiency decreases with decreasing turbine inlet temperature, power production per unit mass of air decreases. Taken into consideration that net power production is important for TES system, lifetime of single bed is selected as 1400 s. The results are presented in Table 10. For the selected storage size, it is estimated that the proposed system can continue to generate electricity 11.22 hours during the night.
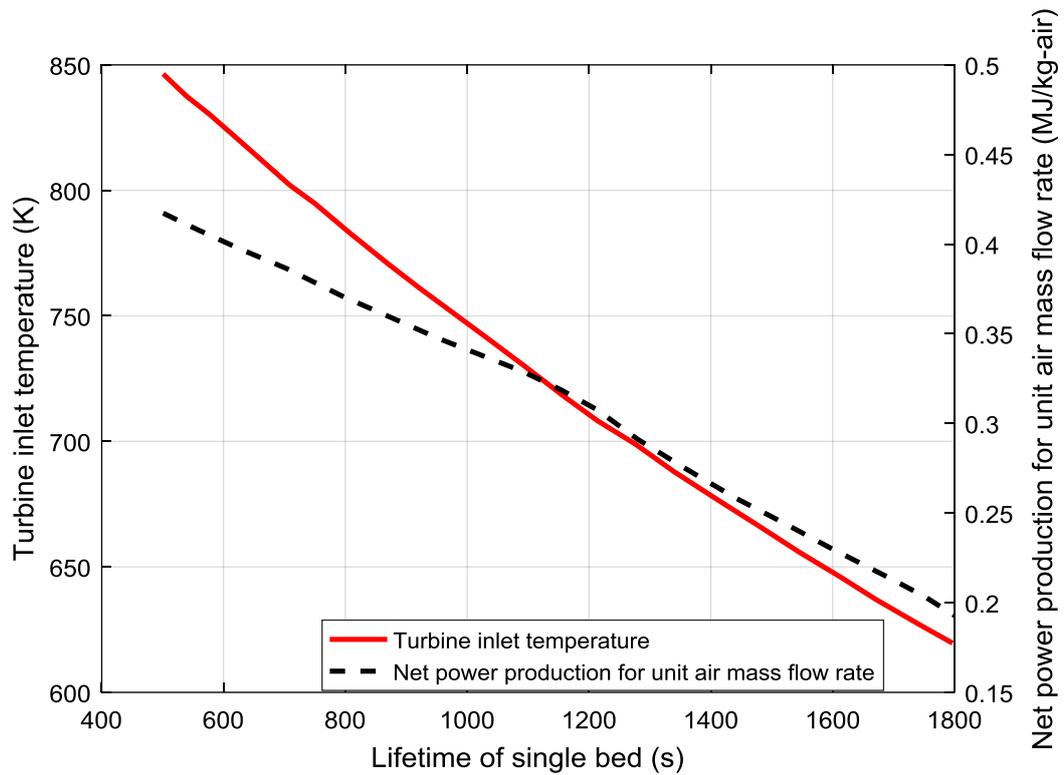

Figure 37. Turbine inlet temperature and net power produced per unit air mass flow rate

Although what-if analysis for Ivanpah Solar Power Plant gives very promising result, there are many practical challenges. First, air Brayton cycle is thermodynamically efficient at high compression ratios, which means high turbine inlet temperature.

However, in this study, turbine inlet temperature is optimized as 679 K, which results in cycle efficiency of 26.4 %. Solugas project [84], which is first megawatt scale solar-hybrid plant, use natural gas combustor to raise the air temperature from 650 °C to 1150 °C. The second and obvious practical challenge is to build more than 6 million beds. To eliminate this problem, up-scaled model is inevitable. Despite these challenges, particle based TES systems are still promising for nest generation CSP systems.

Table 10. Optimization Results

Lifetime of single bed	1400	s
Turbine inlet temperature	679	K
Air mass flow rate	661	kg/s
Net power production	178	MW
Number of active beds	202,962	-
Number of total beds	6,262,843	-
Duration that TES is active	11.22	hours
Cycle Efficiency	0.264	-

CHAPTER 6

CONCLUDING REMARKS

Thermal energy storage is to be integrated with CSP systems to decrease the levelized cost of electricity and increase the capacity factor of the plant. Among the different options for thermal energy storage such as molten salt sensible heat storage, granular materials as a storage medium come to the forefront due to several advantages like high efficiency power cycle, easy handling of material, and material thermal stability in a wide temperature range. Hence, in this study, a bubbling fluidized bed consisting of Geldart B type particles (d_P=275 μm) in a rectangular prism shaped bed is hydrodynamically and thermally modeled to be used as storage medium and direct contact heat exchanger when heat recovery is needed. In modelling and simulations ANSYS Fluent 17.2 is used. In hydrodynamic modelling, Eulerian - Eulerian approach that accepts both phases as continuum, is preferred to avoid high computational power requirement. A mesh size of 5 mm x 5 mm, which corresponds to mesh to particle diameter ratio of 18, gives mesh independent results. For pseudo-2D bed, of which the depth is relatively short compared to other dimensions, 2D modelling gives reasonable pressure drop across the bed although it underestimates the bed expansion, resulting from neglecting the effect of the side walls. Time interval to be used to average the transient model outputs are determined in such a way that the unsteady behavior in first several seconds is neglected.

Syamlal O'Brien drag model, Gidaspow drag model and parameterized Syamlal O'Brien drag model are compared in a quantitative manner. Bed expansion ratio of the bed, voidage profile and pressure drop between different locations are used to validate hydrodynamics. Various restitution coefficient and specularity coefficient values are

75

considered. No significant dependence on these model parameters are observed, but it can be said that as restitution coefficient increases and specularity coefficient decreases, the simulation results slightly better predicts time averaged voidage profiles for Syamlal O'Brien drag model. Parameterized Syamlal – O'Brien drag model, which uses experimentally reported minimum fluidization velocity and voidage as an input, overestimates the bed height, which also results in overestimated temporal voidage profile. Both Gidaspow and Syamlal – O 'Brien drag models are in good agreement with experimental data in terms of bed expansion ratio and pressure drop. Syamlal - O'Brien model could not predict fluidization at low velocities; however, it gives more accurate results at superficial velocities of 0.38 and 0.46 m/s in terms of time averaged voidage profiles.

Interphase heat transfer coefficient is found to be decreasing as the elevation from the bottom of the bed increases. It is observed that temperature of the sand does not vary with spatial coordinates significantly, which can be assumed as constant in further modelling. Air exit temperature are almost same as the bulk particle temperature because only milliseconds are enough for air to reach to particle's temperature. This means that as long as the flow control is achieved, and carryover of the particles out of the bed is prevented, the bubble size, shape and intensity do not affect the thermal behavior of the bed since the effective heat transfer occurs at very bottom of the bed. However, for not insulated beds from the side walls, bubble behavior may affect the wall - to - bed heat transfer coefficient.

The obtained thermal results are used to model a particle based storage system for Ivanpah Solar Power Plant. Air Brayton cycle with efficiency of 0.264 can produce 178 MW electricity during 11.22 hours. For Ivanpah, 26304 metric tons silica sand are required for daily storage.

Although numerical results are promising to make use of bubbling bed as direct contact heat exchanger, there are some practical challenges. The first one is that in real life applications, grains may chip off due to its attrition behavior, which results in smaller grain sizes in cyclic processes. Smaller grain size facilitates the carryover of particles.

In order not to damage the turbine blades, small grains should be filtered, which cause a pressure drop. However, in order to achieve high efficiency in power block, the fluidized bed should be kept at high pressures. Filtering the exit of the bed will cause the fluidized bed to be kept in higher pressures. At this point, sealing of the bed for daily and seasonally storage is an issue. These kind of practical problems should be resolved to make the direct contact heat exchangers feasible in CSP power plants.

6.1. Future Work

These steps will be followed in near future:

- Experiments will be done to validate thermal model. Distinct particle types will be examined in terms of suitability for CSP applications.
- Potential granular materials will be classified according to thermophysical properties.
- The fatigue properties and the lifespan of the granular and ceramic materials will be determined
- Since the fluidized bed should be kept at high pressures, the effect of pressure on hydrodynamics and thermal behavior of the bed will be investigated
- Up-scaled version of the bed will be modeled numerically and experimentally.

Rankine cycle is the state-of-art for power block as of 2017. Air- Brayton cycle and supercritical CO_2, which requires relatively high turbine inlet temperature, is also promising in the near future. Therefore, for supercritical CO_2 cycle, CO_2 can also be considered as fluidizing gas in bed.

REFERENCES

[1]   IRENA (Inernational Renewable Energy Agency), "The Power to Change: Solar and Wind Cost Reduction Potential to 2025," 2016.

[2]   "Türkiye Enerji Görünümü." [Online]. Available: https://www.mmo.org.tr/sites/default/files/TURKIYE ENERJI GORUNUMU_2017_%2825.03%29.pdf. [Accessed: 27-Jun-2016].

[3]   "Solar resource maps for Turkey." [Online]. Available: http://solargis.com/products/maps-and-gis-data/free/download/turkey. [Accessed: 26-Jun-2017].

[4]   P. Kurup and C. Turchi, "Initial Investigation into the Potential of CSP Industrial Process Heat for the Southwest United States," 2015.

[5]   IEA ETSAP and IRENA, "Solar Heat for Industrial Processes - Technology Brief," 2015.

[6]   M. Romero-Alvarez and E. Zarza, "Concentrating Solar Thermal Power," in *Handbook of Energy Efficiency and Renewable Energy*, 2007, p. 21 1-98.

[7]   G. Glatzmaier, "Summary Report for Concentrating Solar Power Thermal Storage Workshop, New Concepts and Materials for Thermal Energy Storage and Heat Transfer Fluids May 20,2011," 2011.

[8]   "Power Tower Projects." [Online]. Available: https://www.nrel.gov/csp/solarpaces/power_tower.cfm. [Accessed: 29-Jun-2017].

[9]   B. Wong, L. Brown, R. Buckingham, D. Thomey, M. Roeb, and C. Sattler, "Concentrating Solar Power Program Review 2013 - Sulfur Based Thermochemical Energy Storage for Solar Power Tower," 2013.

[10]   "Thermochamical heat storage for concentrated solar power - Thermochemical System Reactor Design for Thermal Energy Storage Phase II

Final Report for the period September 30,2008 through April 30,2011," 2011.

[11] K. Lovegrove and W. Stein, *Concentrating Solar Power Technology: Principles, Developments and Applications*. 2012.

[12] L. F. Cabeza, Ed., *Advances in Thermal Energy Storage Systems: Methods and Applications*. 2015.

[13] H. Benoit, I. Perez Lopez, D. Gauthier, J. L. Sans, and G. Flamant, "On-sun demonstration of a 750 C heat transfer fluid for concentrating solar systems: Dense particle suspension in tube," *Sol. Energy*, vol. 118, pp. 622–633, 2015.

[14] C. K. Ho and B. D. Iverson, "Review of high-temperature central receiver designs for concentrating solar power," *Renew. Sustain. Energy Rev.*, vol. 29, pp. 835–846, 2014.

[15] Z. Ma, M. Mehos, G. Glatzmaier, and B. B. Sakadjian, "Development of a concentrating solar power system using fluidized- bed technology for thermal energy conversion and solid particles for thermal energy storage," in *Energy Procedia*, 2015, vol. 69, pp. 1349–1359.

[16] S. Warerkar, S. Schmitz, J. Goettsche, B. Hoffschmidt, M. Reißel, and R. Tamme, "Air-Sand Heat Exchanger for High-Temperature Storage," *J. Sol. Energy Eng.*, vol. 133, pp. 1–8, 2011.

[17] T. Baumann, S. Zunft, and R. Tamme, "Moving Bed Heat Exchangers for Use With Heat Storage in Concentrating Solar Plants: A Multiphase Model," *Heat Transf. Eng.*, vol. 35, no. 3, pp. 224–231, 2013.

[18] F. Taghipour, N. Ellis, and C. Wong, "Experimental and computational study of gas-solid fluidized bed hydrodynamics," *Chem. Eng. Sci.*, vol. 60, no. 24, pp. 6857–6867, 2005.

[19] F. Vejahati, N. Mahinpey, N. Ellis, and M. B. Nikoo, "CFD simulation of gas-solid bubbling fluidized bed: A new method for adjusting drag law," *Can. J. Chem. Eng.*, vol. 87, no. 1, pp. 19–30, 2009.

[20]   D. Kunii and O. Levenspiel, *Fluidization Engineering*. 1991.

[21]   K. S. Lim, J. X. Zhu, and J. R. Grace, "Hydrodynamics of gas-solid fluidization," *Int. J. Multiph. Flow*, vol. 21, no. Suppl., pp. 141–193, 1995.

[22]   W.-C. Yang, "Particle Characterization and Dynamics," in *Handbook of fluidization and fluid-particles systems*, New York, 2003.

[23]   D. Geldart, "Types of gas fluidization," *Powder Technol.*, vol. 7, pp. 285–292, 1973.

[24]   A. Haider and O. Levenspiel, "Drag Coefficient and Terminal Velocity of Spherical and Nonspherical Particles," *Powder Technol.*, vol. 58, pp. 63–70, 1989.

[25]   S. Pannala, M. Syamlal, and T. J. O'Brien, *Computational Gas-Solids Flows and Reacting Systems- Theory, Methods and Practice*. New York, 2011.

[26]   M. Chiesa, V. Mathiesen, J. A. Melheim, and B. Halvorsen, "Numerical simulation of particulate flow by the Eulerian-Lagrangian and the Eulerian-Eulerian approach with application to a fluidized bed," *Comput. Chem. Eng.*, vol. 29, no. 2, pp. 291–304, 2005.

[27]   G. Johnson, M. Massoudi, and K. . Rajagopal, "A review of interaction mechanisms in fluid-solid flows," Pittsburgh, 1990.

[28]   M. Syamlal and T. J. O'Brien, "The Derivation of a Drag Coefficient Formula from Velocity-Voidage Correlations," 1987.

[29]   M. Syamlal and T. J. O'Brien, "Computer simulation of bubbles in a fluidized bed," *AIChE Symp. Ser.*, vol. 85, no. 270, pp. 22–31, 1989.

[30]   M. Syamlal and T. J. O'Brien, "Fluid dynamic simulation of O-3 decomposition in a bubbling fluidized bed," *Aiche J.*, vol. 49, no. 11, pp. 2793–2801, 2003.

[31]   J. Garside and M. R. Al-Dibouni, "Velocity-Voidage Relationships for

Fluidization and Sedimentation in Solid-Liquid Systems," *Ind. Eng. Chem. Process Des. Dev.*, vol. 16, no. 2, pp. 206–214, 1977.

[32]   D. Gidaspow, R. Bezburuah, and J. Ding, "Hydrodynamics of circulating fluidized beds: Kinetic theory approach," *Proc. Seventh Eng. Foundatian Conf. Fluid.*, pp. 75–82, 1992.

[33]   C. Wen and Y. H. Yu, "Mechanics of fluidization," *Chem. Eng. Prog. Symp. Ser.*, vol. 62, pp. 100–111, 1966.

[34]   S. Ergün, "Fluid Flow through Packed Columns," *Chem. Eng. Prog*, vol. 48, no. 2, pp. 89–94, 1952.

[35]   R. Di Felice, "The voidage function for fluid-particle interaction systems," *Int. J. Multiph. Flow*, vol. 20, no. 1, pp. 153–159, 1994.

[36]   H. Arastoopour, P. Pakdel, and M. Adewumi, "Hydrodynamic analysis of dilute gas-solids flow in a vertical pipe," *Powder Technol.*, vol. 62, pp. 163–170, 1990.

[37]   Y. Zhang and J. M. Reese, "The drag force in two-fluid models of gas-solid flows," *Chem. Eng. Sci.*, vol. 58, pp. 1641–1644, 2003.

[38]   L. G. Gibilaro, R. Di Felice, S. P. Waldram, and P. U. Foscolo, "Generalized friction factor and drag coefficient correlations for fluid-particle interactions," *Chem. Eng. Sci.*, vol. 40, no. 10, pp. 1817–1823, 1985.

[39]   R. J. Hill, D. L. Koch, and A. J. C. Ladd, "Moderate-Reynolds-number flows in ordered and random arrays of spheres," *J. Fluid Mech.*, vol. 448, pp. 243–278, 2001.

[40]   *Ansys Fluent Theory Guide 17.0*. 2016.

[41]   C. K. . Lun, S. B. Savage, D. . Jeffrey, and N. Chepurniy, "Kinetic theories for granular flow: inelastic particles in Couette flow and slightly inelastic particles in a general flowfield," *J. Fluid Mech.*, vol. 140, pp. 223–256, 1984.

[42] D. Gidaspow, *Multiphase flow and fluidization - Continuum and Kinetic Theory Descriptions*. 1994.

[43] Ding Jianmin and D. Gidaspow, "A Bubbling Fluidization Model Using Kinetic Theory of Granular Flow," *AIChE J.*, vol. 36, no. 4, pp. 523–538, 1990.

[44] S. Dartevelle, "Numerical and granulometric approaches to geophysical granular flows," Phd. Thesis, Michigan Technology University, 2003.

[45] B. G. M. van Wachem, J. C. Schouten, R. Krishna, and C. M. van den Bleek, "Eulerian simulations of bubbling behaviour in gas-solid fluidised beds," *Comput. Chem. Eng.*, vol. 22, pp. S299–S306, 1998.

[46] M. Syamlal, W. Rogers, and T. J. O`Brien, "MFIX documentation theory guide," Morgantown, 1993.

[47] P. C. Johnson and R. Jackson, "Friction -collisional constitutive relations for granular materials, with application to plane shearing," *J. Fluid Mech.*, vol. 176, pp. 67–93, 1987.

[48] T. Li and S. Benyahia, "Evaluation of Wall Boundary Condition Parameters for Gas–Solids Fluidized Bed Simulations," *AIChE J.*, vol. 59, no. 10, pp. 3624–3632, 2013.

[49] D. J. Gunn, "Transfer of heat or mass to particles in fixed and fluidised beds," *Int. J. Heat Mass Transf.*, vol. 21, no. 4, pp. 467–476, 1978.

[50] M. Diago, A. C. Iniesta, T. Delclos, A. Soum-glaude, T. Shamim, M. Diago, A. C. Iniesta, and T. Delclos, "Characterization of Desert Sand as a Sensible Thermal Energy Storage Medium," in *SolarPACES*, 2015, vol. 50011, pp. 1–9.

[51] T. Baumann and S. Zunft, "Properties of granular materials as heat transfer and storage medium in CSP application," *Sol. Energy Mater. Sol. Cells*, vol. 143, pp. 38–47, 2015.

[52] P. Jund and R. Jullien, "Molecular-dynamics calculation of the thermal conductivity of vitreous silica ´," *Am. Phys. Soc.*, vol. 59, no. 21, pp. 707–711, 1999.

[53] H. Enwald, E. Peirano, A. E. Almstedt, and B. Leckner, "Simulation of the fluid dynamics of a bubbling fluidized bed. Experimental validation of the two-fluid model and evaluation of a parallel multiblock solver," *Chem. Eng. Sci.*, vol. 54, no. 3, pp. 311–328, 1999.

[54] E. Peirano, V. Delloume, and B. Leckner, "Two- or three-dimensional simulations of turbulent gas-solid flows applied to fluidization," *Chem. Eng. Sci.*, vol. 56, pp. 4787–4799, 2001.

[55] M. J. V Goldschmidt, J. A. M. Kuipers, and W. P. M. Van Swaaij, "Hydrodynamic modelling of dense gas-fluidised beds using the kinetic theory of granular flow: Effect of coefficient of restitution on bed dynamics," *Chem. Eng. Sci.*, vol. 56, pp. 571–578, 2001.

[56] B. van Wachem, J. C. Schouten, C. M. Van Den Bleek, R. Krishna, and Sinclair J. L., "Comparative Analysis of CFD Models of Dense Gas − Solid Systems," *AIChE J.*, vol. 47, no. 5, pp. 1035–1051, 2001.

[57] B. Halvorsen and V. Mathiesen, "CFD Modelling and simulation of a lab scale Fluidised Bed," *Model. Identif. Control*, vol. 23, no. 2, pp. 117–133, 2002.

[58] L. Huilin, H. Yurong, and D. Gidaspow, "Hydrodynamic modelling of binary mixture in a gas bubbling fluidized bed using the kinetic theory of granular flow," *Chem. Eng. Sci.*, vol. 58, no. 7, pp. 1197–1205, 2003.

[59] S. J. Gelderbloom, D. Gidaspow, and R. W. Lyczkowski, "CFD Simulations of Bubbling / Collapsing Fluidized Beds for Three Geldart Groups," *AIChE J.*, vol. 49, no. 4, pp. 844–858, 2003.

[60] J. Lundberg and B. M. Halvorsen, "A review of some exsisting drag models describing the interaction between phases in a bubbling fluidized bed," in

Proc. 49th Scand. Conf. Simulation and Modeling, 2008.

[61] M. Hamzehei and H. Rahimzadeh, "Experimental and Numerical Study of Hydrodynamics with Heat Transfer in a Gas−Solid Fluidized-Bed Reactor at Different Particle Sizes," *Ind. Eng. Chem. Res.*, vol. 48, no. 6, pp. 3177–3186, 2009.

[62] M. Deza, N. P. Franka, T. J. Heindel, and F. Battaglia, "CFD Modeling and X-Ray Imaging of Biomass in a Fluidized Bed," *J. Fluids Eng.*, vol. 131, p. 111303, 2009.

[63] W. Duangkhamchan, F. Ronsse, F. Depypere, K. Dewettinck, and J. G. Pieters, "Comparison and evaluation of interphase momentum exchange models for simulation of the solids volume fraction in tapered fluidised beds," *Chem. Eng. Sci.*, vol. 65, no. 10, pp. 3100–3112, 2010.

[64] F. Battaglia, J. a England, S. Kanholy, and M. Deza, "On the Modeling of Gas-Solid Fluidization : Which Physics Are Most Important To Capture," in *Proceedings of the ASME 2010 International Mechanical Engineering Congress & Exposition IMECE2010*, 2010.

[65] H. J. Krautz, M. Schreiber, and T. W. Asegehegn, "Numerical Study of Bubbling Fluidized Beds: Influence of Immersed Tubes, Extraction Methods and Averaging Periods," in *The 13th International Conference on Fluidization - New Paradigm in Fluidization Engineering*, 2010.

[66] T. W. Asegehegn, M. Schreiber, and H. J. Krautz, "Numerical Simulation of Dense Gas-Solid Multiphase Flows Using Eulerian-eulerian Two-fluid model," in *Computational Simulations and Applications*, 2011.

[67] A. Acosta-Iborra, C. Sobrino, F. Hernández-Jiménez, and M. de Vega, "Experimental and computational study on the bubble behavior in a 3-D fluidized bed," *Chem. Eng. Sci.*, vol. 66, no. 15, pp. 3499–3512, 2011.

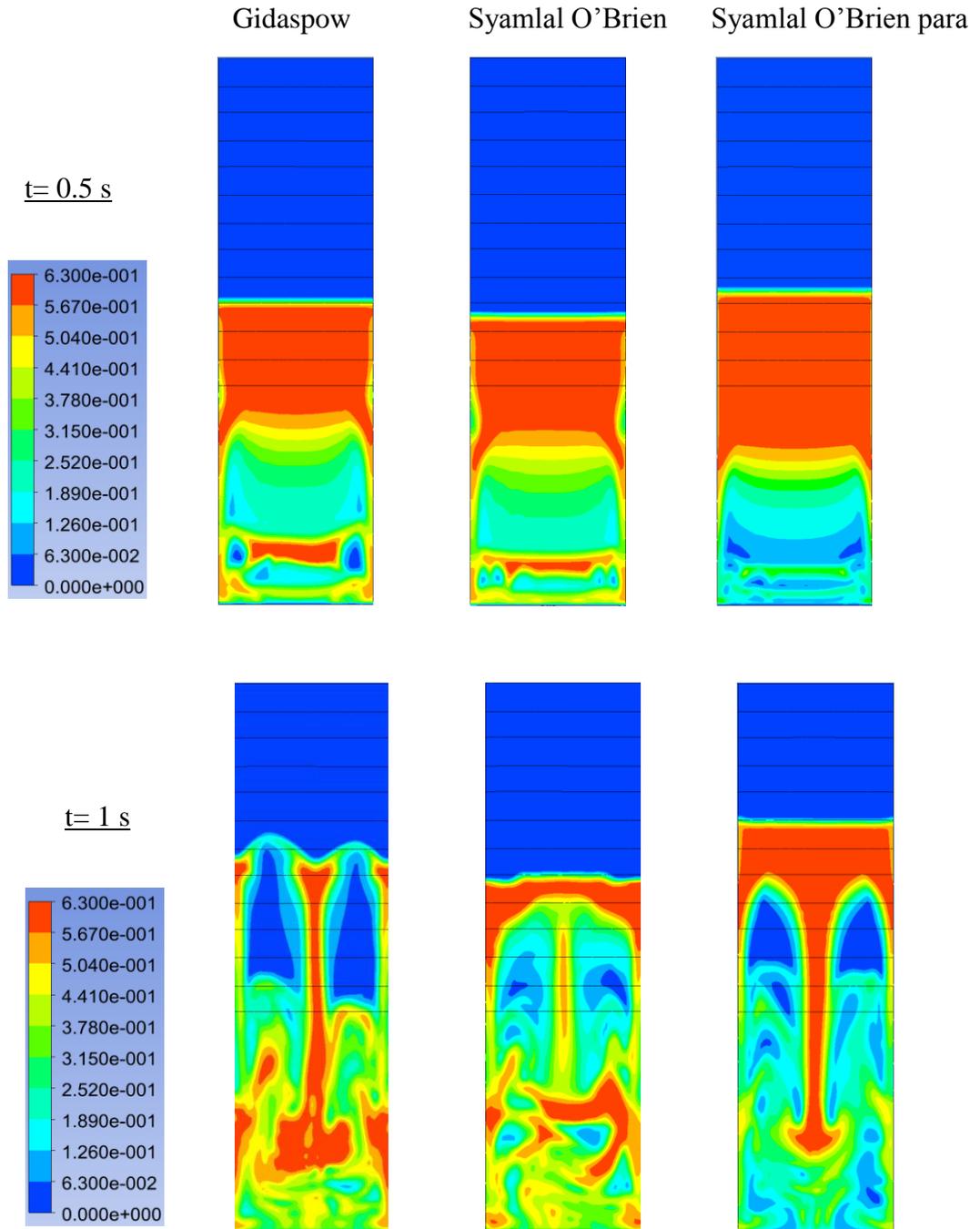[68] F. Hernández-Jiménez, S. Sánchez-Delgado, A. Gómez-García, and A.

Acosta-Iborra, "Comparison between two-fluid model simulations and particle image analysis & velocimetry (PIV) results for a two-dimensional gas-solid fluidized bed," *Chem. Eng. Sci.*, vol. 66, no. 17, pp. 3753–3772, 2011.

[69]   N. Herzog, M. Schreiber, C. Egbers, and H. J. Krautz, "A comparative study of different CFD-codes for numerical simulation of gas-solid fluidized bed hydrodynamics," *Comput. Chem. Eng.*, vol. 39, pp. 41–46, 2012.

[70]   C. Loha, H. Chattopadhyay, and P. K. Chatterjee, "Effect of coefficient of restitution in Euler-Euler CFD simulation of fluidized-bed hydrodynamics," *Particuology*, vol. 15, pp. 170–177, 2014.

[71]   S. Patankar, *Numerical heat transfer and fluid flow*. 1980.

[72]   S. Bilyaz, "Numerical investigation of circulating fluidized bed riser hydrodynamics for concentrating solar thermal receiver applications," MSc Thesis, METU, Ankara, 2015.

[73]   C. Tagliaferri, L. Mazzei, P. Lettieri, A. Marzocchella, G. Olivieri, and P. Salatino, "CFD simulation of bubbling fluidized bidisperse mixtures: Effect of integration methods and restitution coefficient," *Chem. Eng. Sci.*, vol. 102, pp. 324–334, 2013.

[74]   P. Sahoo and A. Sahoo, "A Comparative Study on Effect of Different Parameters of CFD Modeling for Gas–Solid Fluidized Bed," *Part. Sci. Technol.*, vol. 33, pp. 273–289, 2015.

[75]   T. W. Asegehegn, M. Schreiber, and H. J. Krautz, "Numerical simulation and experimental validation of bubble behavior in 2D gas-solid fluidized beds with immersed horizontal tubes," *Chem. Eng. Sci.*, vol. 66, pp. 5410–5427, 2011.

[76]   H. Askaripour and A. Molaei Dehkordi, "Simulation of 3D freely bubbling gas–solid fluidized beds using various drag models: TFM approach," *Chem. Eng. Res. Des.*, vol. 100, pp. 377–390, 2015.

[77]   L. Mazzei and P. Lettieri, "CFD simulations of expanding/contracting

homogeneous fluidized beds and their transition to bubbling," *Chem. Eng. Sci.*, vol. 63, pp. 5831–5847, 2008.

[78]   C. Loha, H. Chattopadhyay, and P. K. Chatterjee, "Assessment of drag models in simulating bubbling fluidized bed hydrodynamics," *Chem. Eng. Sci.*, vol. 75, pp. 400–407, 2012.

[79]   S. Zimmermann and F. Taghipour, "CFD modeling of the hydrodynamics and reaction kinetics of FCC fluidized-bed reactors," *Ind. Eng. Chem. Res.*, vol. 44, pp. 9818–9827, 2005.

[80]   J. R. Grace and F. Taghipour, "Verification and validation of CFD models and dynamic similarity for fluidized beds," *Powder Technol.*, vol. 139, pp. 99–110, 2004.

[81]   M. Lungu, J. Sun, J. Wang, Z. Zhu, and Y. Yang, "Computational fluid dynamics simulations of interphase heat transfer in a bubbling fluidized bed," *Korean J. Chem. Eng.*, vol. 31, no. 7, pp. 1148–1161, 2014.

[82]   C. van Heerden, A. P. P. Nobel, and D. W. van Krevelen, "Mechanism of Heat Transfer in Fluidized Beds," *Ind. Eng. Chem.*, vol. 45, no. 6, pp. 1237–1242, 1953.

[83]   F. P. Incropera, D. P. Dewitt, T. L. Bergman, and A. S. Lavine, *Fundamentals of Heat and Mass Transfer*, 7th ed. .

[84]   R. Korzynietz, J. A. Brioso, A. Río, M. Quero, M. Gallas, R. Uhlig, M. Ebert, R. Buck, and D. Teraji, "Solugas – Comprehensive analysis of the solar hybrid Brayton plant," *Sol. Energy*, vol. 135, pp. 578–589, 2016.

APPENDICES

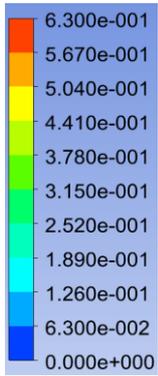## A. Solid Volume Fraction Contour for Distinct Drag Models at Different Simulation Times

U= 0.38 m/s

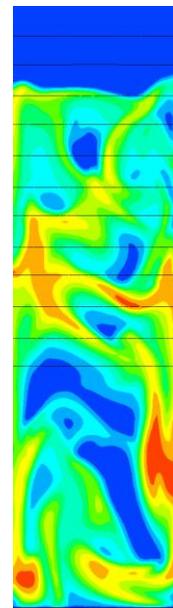| Gidaspow | Syamlal O'Brien | Syamlal O'Brien para |

t= 0.5 s

t= 1 s

Gidaspow   Syamlal O'Brien   Syamlal O'Brien para

t= 1.5 s

| 6.300e-001 |
| 5.670e-001 |
| 5.040e-001 |
| 4.410e-001 |
| 3.780e-001 |
| 3.150e-001 |
| 2.520e-001 |
| 1.890e-001 |
| 1.260e-001 |
| 6.300e-002 |
| 0.000e+000 |

t= 2 s

| 6.300e-001 |
| 5.670e-001 |
| 5.040e-001 |
| 4.410e-001 |
| 3.780e-001 |
| 3.150e-001 |
| 2.520e-001 |
| 1.890e-001 |
| 1.260e-001 |
| 6.300e-002 |
| 0.000e+000 |

90

U= 0.46 m/s

Gidaspow   Syamlal O'Brien   Syamlal O'Brien para

t= 1.5 s

| 6.300e-001 |
| 5.670e-001 |
| 5.040e-001 |
| 4.410e-001 |
| 3.780e-001 |
| 3.150e-001 |
| 2.520e-001 |
| 1.890e-001 |
| 1.260e-001 |
| 6.300e-002 |
| 0.000e+000 |

t= 2 s

| 6.300e-001 |
| 5.670e-001 |
| 5.040e-001 |
| 4.410e-001 |
| 3.780e-001 |
| 3.150e-001 |
| 2.520e-001 |
| 1.890e-001 |
| 1.260e-001 |
| 6.300e-002 |
| 0.000e+000 |

8